International Journal of Hydrogen Energy 249 (2026) 155916

Contents lists available at ScienceDirect

International Journal of Hydrogen Energy

journal homepage: www.elsevier.com/locate/he

Trimetallic MnCo-LDH@NiS–Ni_3S_2/NF heterogeneous nano-skeleton as a high-performance bifunctional electrocatalyst for efficient alkaline overall water splitting

Ujjwal Phadikar [a,b], Anjan Chakraborty [a,b], Srijib Das [a,b], Debasish Mondal [c], Sukanya Bhattacharjee [a,b], Debasis Dhak [c], Naresh Chandra Murmu [a,b], Tapas Kuila [a,b,*]

[a] Electric Mobility and Tribology Research Group (EM&TRG), Council of Scientific and Industrial Research-Central Mechanical Engineering Research Institute, Durgapur, 713209, India
[b] Academy of Scientific and Innovative Research (AcSIR), Ghaziabad, 201002, India
[c] Department of Chemistry, Sidho-Kanho-Birsha University, Purulia, 723104, India

ARTICLE INFO

Keywords:
Heterostructure
In-situ growth
Heterointerface
HER
OER
Alkaline water electrolysis

ABSTRACT

This research presents a multi-metallic, hierarchical MnCo-LDH@NiS–Ni_3S_2/NF (MCNS/NF) heterostructure, prepared via a two-step hydrothermal approach. The XRD, HR-TEM, AC-HAADF-STEM imaging, EELS analysis, and line-scan elemental mapping confirmed the formation of a well-defined heterostructure framework that could enhance the intrinsic electrocatalytic efficiency, thereby leading to stellar performance in alkaline water electrolysis. The as-prepared catalyst exhibited efficient gas evolution during both the hydrogen evolution reaction (HER) and oxygen evolution reaction (OER), delivering ultralow overpotentials of 83 mV for HER and 230 mV for OER, respectively, at a current density of 10 mA cm^{-2} in 1.0 M KOH. Additionally, the assembled two-electrode system achieved a minimum cell voltage of 1.54 V at the same current density, Faradaic efficiencies of 93.02% for H_2 & 91.90% for O_2, and long-term operational stability. Henceforth, these fascinating outcomes shed light on the rationally designed heterostructure for alkaline water electrolysis application.

1. Introduction

Alongside the emergence of living prototypes and industrial technologies, there is a rapid depletion of non-renewable resources, primarily fossil fuels [1–3]. Various energy conversion (EC) technologies have been developed to meet the surge in demand for sustainable energy in an eco-friendly manner and to reduce reliance on non-renewable resources [4,5]. Hence, EC technologies have sparked significant research interest in conserving electrical energy from renewable energy resources [6–11]. The rational design of multifunctional electrocatalysts is crucial to achieve high-performance water-splitting processes for sustainable H_2 production [12–18]. Recently, the controllable integration of HER, OER, and OWS electrocatalysts into a single multi-metallic hybrid nanostructure, leveraging the inherent advantages of each component, has demonstrated enhanced electrocatalytic performance [19,20]. Therefore, tuning the subtle balance between water dissociation and the subsequent chemisorption of reaction intermediates on electrode surfaces is crucial for assessing the kinetics of HER, OER, and OWS in an alkaline medium [21–23]. Accordingly, this work focuses on the development of a bifunctional electrocatalyst with a multi-component architecture, aiming to improve electrocatalytic activity for alkaline water splitting by enhancing charge-transfer properties and increasing the exposure of electrochemically active sites. To date, noble Pt-based carbon materials and Ru/Ir-based precious electrocatalysts remain the most efficient for advanced HER and OER applications. However, their low abundance, high cost, and short-term durability significantly restrict their use in commercial H_2 production [24,25]. Hence, swapping these noble metals with highly efficient, inexpensive, environmentally friendly, non-noble-metal-based electrocatalysts holds significant potential in electrocatalysis. In this regard, transition metal sulfides are emerging materials that have garnered considerable attention due to their tunable electronic structure, uncompromised electrical conductivity, and appropriately filled energy gap [26,27]. Surprisingly, numerous investigations have revealed that transition metal sulfide

* Corresponding author. Electric Mobility and Tribology Research Group (EM&TRG), Council of Scientific and Industrial Research-Central Mechanical Engineering Research Institute, Durgapur, 713209, India.
E-mail address: tkuila.cmeri@csir.res.in (T. Kuila).

https://doi.org/10.1016/j.ijhydene.2026.155916
Received 9 March 2026; Received in revised form 2 June 2026; Accepted 4 June 2026
Available online 13 June 2026

(TMS)-based electrocatalysts are the promising choice for HER catalysis, owing to their hydrogenase-like catalytic mechanism. However, its OER performance is significantly restricted, and in turn, reduces its anodic performance potential due to the lack of abundant active sites. Dissolution of sulfur damages the surface reactive sites [28]. Consequently, there is an urgent need to strategically alter the morphology and nanostructure of the electrocatalysts to expose abundant surface-active sites and accelerate electron-transport rates [29]. Therefore, it has been documented that the selective construction of heterojunctions cannot only integrate the intrinsic advantages of different components but also accelerate the transfer of ions and electrons [30]. Furthermore, coupling the inner-phase material wrapped in the outer phase with a heterostructured electrocatalyst can also shorten the diffusion path, thereby enhancing conductivity. Additionally, the outer phase material can protect the inner phase material and provide a unique morphology, thereby promoting significant mass transfer efficiency [31,32]. Apart from the various types of prevalent inner phase-type electrode materials, two-dimensional (2D) layered double hydroxides (LDHs) have emerged as a research hotspot owing to their large specific surface area, admirable stability, flexible open electronic structure, most optimal M − O bond strength, adjustable tunability, rich redox properties, good anion exchange behaviour, and extraordinary catalytic activity towards OER [33,34]. However, its metastable structure inherently exhibits poor electrical conductivity, attributed to the completely occupied $MO_{6\text{-}x}$ center, which is tethered to the t_{2g} orbital, rendering it unattainable to achieve the theoretical OER kinetics [35]. On the other hand, in the case of LDHs, the interlayer spacing is constrained, and there is a degree of steric hindrance and electrostatic attraction between the layers. Consequently, the restricted interlayer space will affect the diffusion paths of molecules or ions when they need to diffuse between the layers, and their electrostatic attraction will trigger the ions or molecules to interact strongly with the laminates, thereby enhancing the difficulty of diffusion and resulting in a decrease in mass diffusion rate [36]. Based on the above discussion, the limitation can be mitigated through hierarchical heterostructure integration, which brings new potential. This approach enables breaking bottlenecks and tailoring the electronic structure to effectively enhance electron-migration kinetics at intimate sites by reducing interfacial contact resistance. Generally, a 2D-LDH nanosheet ensures strong integration between the electrode material and the supporting substrate, offering a large surface area [37]. Meanwhile, the 1D-TMS is employed as an outer phase to provide abundant surface sites, various oxidation states, and undergo diverse redox reactions, which facilitate efficient charge-transfer kinetics and have been shown to maintain high electrocatalytic activity [38,39]. Such a combination of different dimensionality holds great promise as a material for interconnected 3D networks, which will be reflected in improved overall electrochemical efficiency for alkaline water electrolysis. This design strategy is further supported by recent literature on Ni foam-supported LDH@metal sulfide heterostructures, as summarized in Table S1. For instance, Chen et al. reported a Co_3S_4@NiFe-LDH core-shell heterostructure, where the strong synergistic coupling between the sulfide core and LDH shell effectively enhanced charge-transfer kinetics, delivering an HER overpotential of 95 mV, an OER overpotential of 235 mV, and OWS cell voltage of 1.595 V. Similarly, Zhang et al. developed a three-dimensional walnut-like Mo–Ni_3S_2@NiFe LDH catalyst, in which the hierarchical porous architecture and abundant heterointerfaces facilitated rapid ion/electron transport and improved catalytic accessibility, resulting in an HER overpotential of 153 mV, an OER overpotential of 331 mV, and an OWS cell voltage of 1.57 V. Zhao et al. synthesized a NiAl-LDH/Ni_3S_2 nanocomposite that exhibited highly efficient bifunctional behavior with an HER overpotential of 53.6 mV, an OER overpotential of 350.4 mV, and an OWS cell voltage of 1.56 V, highlighting the synergistic effect of LDH-sulfide coupling for hydrogen evolution. Furthermore, Ye et al. constructed crystalline-amorphous Ni_xS_y@NiFe LDH heterojunctions, where defect-rich interfacial regions optimized intermediate adsorption and enhanced catalytic kinetics, achieving HER and OER overpotentials of 159 mV and 250 mV (at 100 and 200 mA cm^{-2}, respectively). In addition, Yang et al. fabricated self-supported NiFe-LDH@CoS_x nanosheet arrays with a vertically aligned architecture and strong interfacial contact, promoting efficient electron transport and gas release and yielding an HER overpotential of 136 mV, an OER overpotential of 206 mV, and an OWS cell voltage of 1.537 V. Moreover, Han et al. developed Ni_3S_2-Ni_xP_y@NiFe LDH heterogeneous nanoflowers with a well-engineered 3D architecture, delivering a low OWS cell voltage of 1.54 V due to enhanced mass transport and abundant active interfaces.

Building on prior research, this work proposed a facile and controllable two-step hydrothermal approach to successfully design a novel multi-component 3D-hierarchical MnCo-LDH@NiS–Ni_3S_2/NF heterostructure electrocatalyst, composed of MnCo-LDH nanosheets with vertically stacked hierarchical nanoflower-like NiS–Ni_3S_2 hybrids. Furthermore, the key novelties of the present work are summarized as follows: (a) A rationally engineered, interface-rich, hierarchical 3D-interconnected MnCo-LDH@NiS–Ni_3S_2/NF heterostructure is developed via a facile two-step hydrothermal strategy, as evidenced by PXRD, HR-TEM, advanced AC-HAADF-STEM imaging, EELS analysis, line-scan elemental mapping, and HR-TEM measurements, which integrates LDHs and metal-sulfide phases grown directly on NF. (b) Explicit structural engineering at the enriched multi-heterointerface is introduced to induce the conductivity. This heterointerface design generates a large number of metal-active sites, thereby effectively enhancing the electrochemically active surface area and intrinsic electrocatalytic activity. (c) In accordance, the bifunctional capability within a single noble-metal-free electrode has been demonstrated, encompassing efficient HER and OER. Therefore, the current study proposed a revolutionary design paradigm for long-term improvement in high-performance rationally designed heterostructure electrocatalysts to boost industrial-scale green H_2 production, future energy conversion systems, and go beyond incremental gains over prior efforts.

2. Experimental section

2.1. Reagents, physicochemical characterization, and electrochemical measurements

The electronic supplementary information provides a comprehensive overview of the materials, chemical reagents, physicochemical characterization techniques, and electrochemical measurement parameters employed in this study (Section S1-S3).

2.2. Pre-treatment for bare-Nickel foam (NF)

Prior to the growth of electrode materials, the surface oxide layer was thoroughly removed from commercially available NF. The cleaning process began with ultrasonication in acetone for 30 min to dissolve organic contaminants, followed by sequential rinsing with deionized (DI) water and absolute ethanol to eliminate any remaining residues. After cleaning, the NF pieces were sealed and stored for subsequent use.

2.3. Synthesis of honeycomb-like MnCo-LDH/NF nanosheet arrays

To synthesize honeycomb-like MnCo-LDH/NF nanosheet arrays, first, $Mn(NO_3)_2{\cdot}4H_2O$ (3 mmol), $Co(NO_3)_2{\cdot}6H_2O$ (1 mmol), urea (10 mmol), and tri-sodium citrate (0.33 mmol) were dissolved in 70 ml of DI water at room temperature. Then, a mixed homogeneous solution and a piece of pre-treated NF were placed in a 100 mL Teflon-lined autoclave and heated to 125 °C for 15 h. After natural cooling, the LDH-coated NF was rinsed several times with DI water and anhydrous ethanol, then vacuum-dried at 50 °C overnight. The growth process of the honeycomb-like MnCo-LDH/NF nanosheet arrays is schematically depicted in Fig. S1. The obtained MnCo-LDH/NF was subsequently incorporated into hierarchical nanoflower-like NiS–Ni_3S_2 nanoarrays to

develop a hybrid heterostructure.

2.4. Synthesis of NiS–Ni_3S_2/NF and MnCo-LDH@NiS–Ni_3S_2/NF arrays

Hierarchical nanoflower-like NiS–Ni_3S_2/NF and marigold-flower-like heterogeneous MnCo-LDH@NiS–Ni_3S_2/NF nanoarrays were prepared via a facile one-pot hydrothermal method. To synthesize the NiS–Ni_3S_2/NF nanoarrays, pre-treated NF was used as both a supportive substrate and a reactant (source of Ni). In brief, 6 mmol of CH_4N_2S was added to 60 mL of DI water, and the mixture was stirred for 1 h. Subsequently, a piece of pre-treated NF and the above solution were placed into a 100 ml Teflon-lined autoclave reactor. Finally, the NiS–Ni_3S_2/NF was synthesized at 180 °C for 16 h. After the hydrothermal reaction, the autoclave was cooled naturally to room temperature, and the resultant hierarchical, black-colored NF containing NiS–Ni_3S_2 nanoarrays was rinsed alternately with DI water and anhydrous ethanol to remove residual debris, followed by vacuum drying overnight at 50 °C. Similarly, the marigold-flower-like heterogeneous MnCo-LDH@NiS–Ni_3S_2/NF nanoarrays were synthesized using the aforementioned hydrothermal procedure. Herein, instead of bare pre-treated NF, the synthesized MnCo-LDH/NF was immersed in a homogeneous solution of CH_4N_2S (6 mmol) in a Teflon-lined stainless steel autoclave reactor to grow NiS–Ni_3S_2/NF nanoarrays on the surface of MnCo-LDH/NF nanosheet arrays. The brownish, heterogeneous electrocatalyst obtained was designated as MCNS/NF. The developed strategy for preparing these electrocatalysts is schematically depicted in Fig. 1 and S2.

3. Results and discussion

3.1. Proposed mechanistic insights into electrocatalyst nucleation and growth

Based on the aforementioned experiment, the overall synthetic scheme for the marigold-flower-like hybrid heterogeneous MCNS/NF electrocatalyst is shown in Fig. 1. The fabrication flow chart for the heterogeneous MCNS/NF electrocatalyst indicates that hierarchical nanoflower-like NiS–Ni_3S_2 nanoarrays were inserted into honeycomb-like MnCo-LDH/NF nanosheet arrays, forming a self-supported electrode material and creating a MnCo-LDH/NF-encapsulated NiS–Ni_3S_2 heterostructure. Firstly, a plausible growth mechanism for the formation of uniformly reticulated MnCo-LDH nanosheet arrays on the surface of a highly interconnected, three-dimensional NF skeleton with a porous structure is suggested as follows (Equations (1)–(10), and Section S4).

$$CO(NH_2)_2 + 3H_2O \rightarrow 2NH_4^+ + CO_3^{2-} + 2OH^- \quad (1)$$

$$(NH_4)_2CO_3 \rightarrow 2NH_3\uparrow + CO_2\uparrow + H_2O \quad (2)$$

$$NH_3 + H_2O \rightleftharpoons NH_4^+ + OH^- \quad (3)$$

$$CO_2 + H_2O \rightleftharpoons H^+ + HCO_3^- \rightleftharpoons 2H^+ + CO_3^{2-} \quad (4)$$

$$Mn^{2+} + CO_3^{2-} \rightarrow MnCO_3\downarrow \quad (5)$$

$$Co^{2+} + 2OH^- \rightarrow Co(OH)_2 \quad (6)$$

$$Co(OH)_2 + 2(C_6H_5O_7)^{3-} \rightleftharpoons Co[(C_6H_5O_7)_2]^{4-} + 2OH^- \quad (7)$$

$$Co[(C_6H_5O_7)_2]^{4-} \rightleftharpoons Co^{2+} + 2(C_6H_5O_7)^{3-} \quad (8)$$

$$MnCO_3 \rightleftharpoons Mn^{2+} + CO_3^{2-} \quad (9)$$

$$3Mn^{2+} + Co^{2+} + 3CO_3^{2-} + 6OH^- + 6H_2O \rightarrow [Mn_3Co(OH)_6(CO_3)_3]\cdot 6H_2O \quad (10)$$

Consequently, the detailed mechanisms of formation and sulfidation of encapsulated NiS–Ni_3S_2 phases are presented in Equations (11)–(16) and Section S4.

$$CS(NH_2)_2 + 2H_2O \rightarrow 2NH_3 + CO_2 + H_2S \quad (11)$$

$$Ni^{2+} + 4NH_3 \rightarrow [Ni(NH_3)_4]^{2+} \quad (12)$$

$$NH_3 + H_2O \rightarrow OH^- + NH_4^+ \quad (13)$$

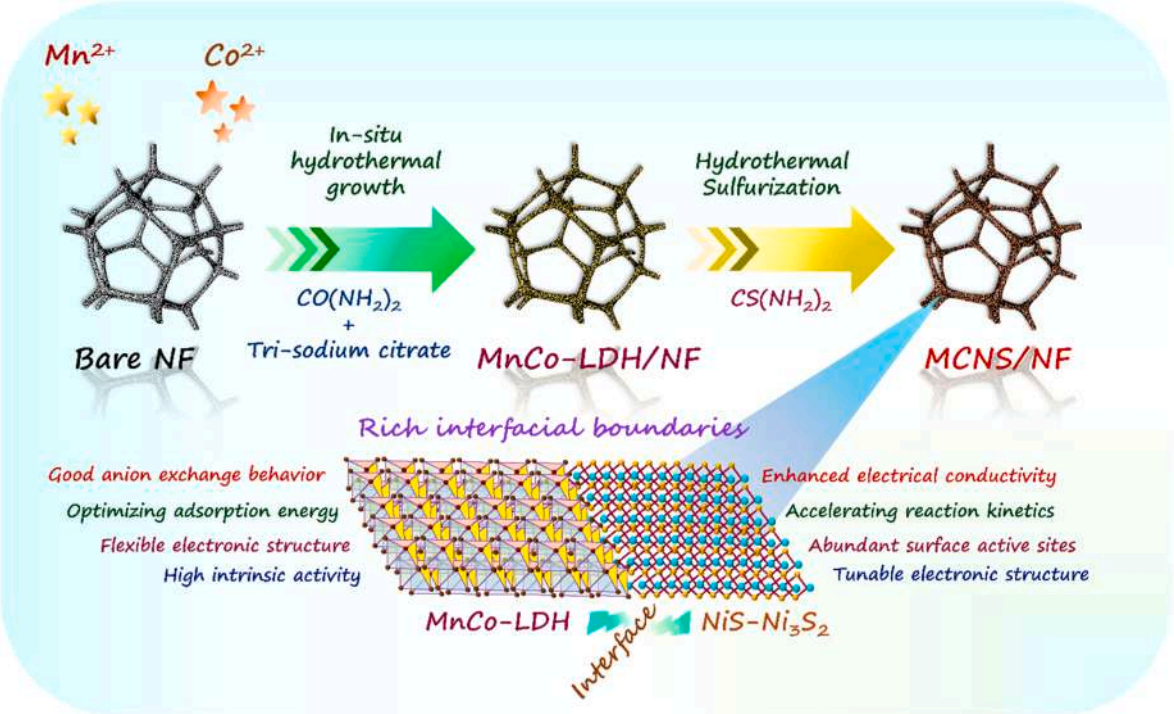

Fig. 1. Schematic of the synthesis of a hierarchical MCNS/NF heterostructure.

$$H_2S + 2OH^- \rightarrow S^{2-} + 2H_2O \quad (14)$$

$$[Ni(NH_3)_4]^{2+} + S^{2-} \rightarrow NiS + 4NH_3 \quad (15)$$

$$3[Ni(NH_3)_4]^{2+} + 2S^{2-} \rightarrow Ni_3S_2 + 12NH_3 \quad (16)$$

Another significant aspect is that the structural integrity of the MnCo-LDH nanosheets phase was preserved during the secondary hydrothermal sulfidation, where CH_4N_2S served as a limited sulfur source, providing a controlled, slow-release of sulfur source at these mild temperatures (Equation (11)) [33]. In the entire synthesis process, the sulfur chemical potential is insufficient to drive complete anion exchange or bulk phase transformation of MnCo-LDH into metal sulfides because, from a kinetic standpoint, the layered hydroxide lattice of MnCo-LDH possesses strong metal-oxygen bonding within the brucite-like layers and a relatively slow solid-state diffusion rate for sulfur species [40–42]. The transformation of a metal hydroxide into a metal sulfide depends on the solubility product of LDHs and the activation energy of the phase transition. As a result, in the two-step hydrothermal approach, sulfuration is surface-limited and diffusion-controlled, occurring preferentially at the labile Ni-precursor species where Ni^{2+} ions readily reacted with released S^{2-} in the solution to nucleate the thermodynamically favourable NiS–Ni_3S_2 phase on the LDH surface [43–45]. Therefore, this competitive sulfide nucleation on NF further suppresses deep sulfur penetration into the LDH lattice, stabilizing the LDH phase. Benefiting from the efficient heterostructure design, the electronic structure was induced by differences in electronegativity, electronic conductivity, and bonding environments between the metal-oxygen framework of

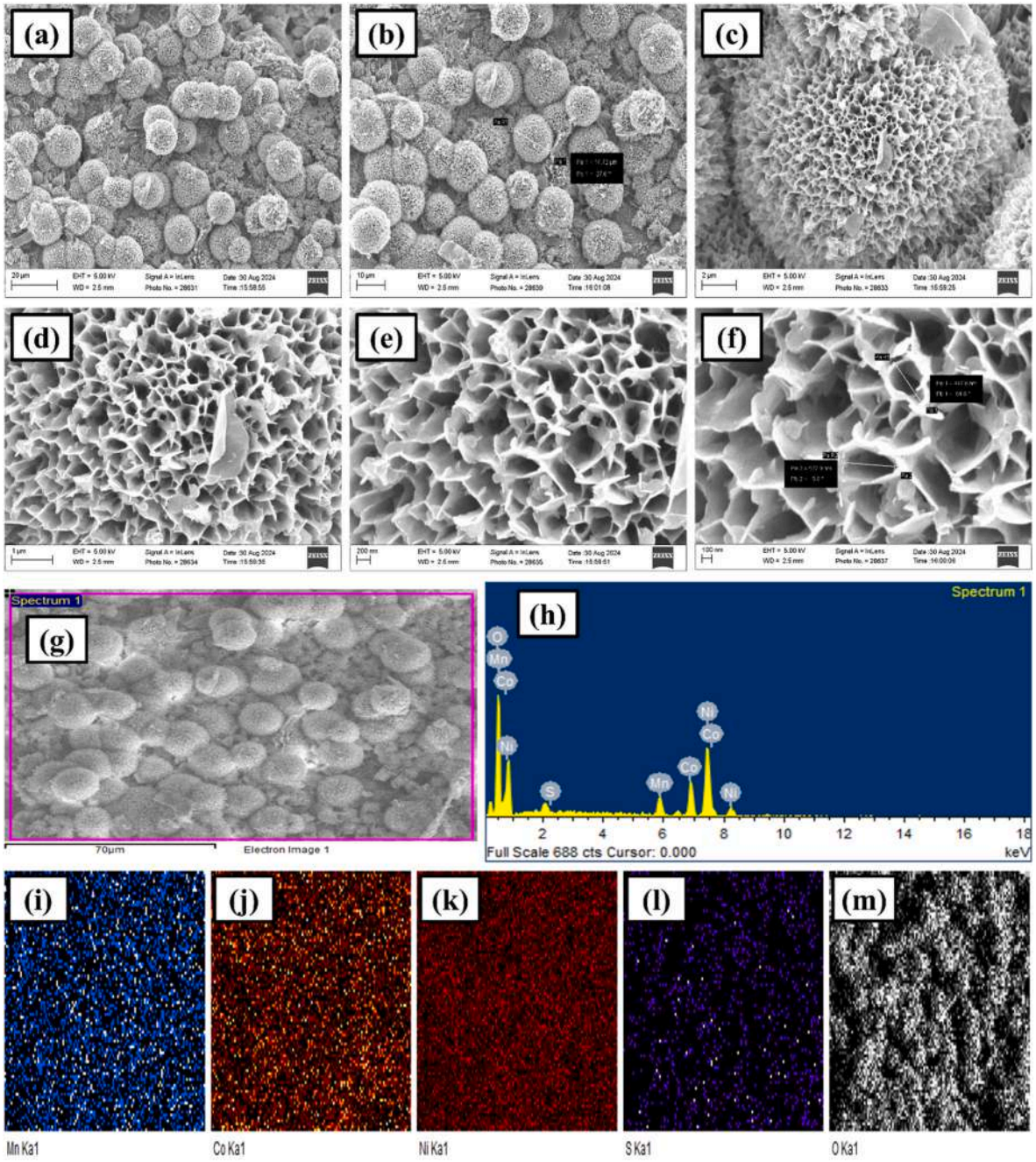

Fig. 2. FE-SEM images of MCNS/NF heterostructure. electrocatalyst at low and high magnification (a-f); FE-SEM-EDX and associated EDX color mapping for Mn, Co, Ni, S, and O, respectively (g-m). (For interpretation of the references to color in this figure legend, the reader is referred to the Web version of this article.)

MnCo-LDH nanosheets and the metal-sulfur motif of NiS–Ni_3S_2 nanoarray. When the two phases are coupled, electrons preferentially redistribute from the more metallic and electron-rich NiS–Ni_3S_2 phase toward the LDH phase, leading to the formation of a heterostructure by partial oxidation of Ni sites in NiS–Ni_3S_2 and stabilization of higher-valence Mn/Co sites at the LDH phase. This charge-transfer and mixed-valence configuration is well known to be electrochemically more active than its single-valence counterparts. Furthermore, the intimate contact reduces the charge-transfer resistance, thereby facilitating rapid electron transport across the heterojunction. This spatially integrated hetero-nanostructured framework, inheriting strong electrocatalytic properties, provided a high electrochemically active surface area and promoted the exposure of active sites. Benefiting from an efficient interface design, the prepared hybrid electrocatalyst exhibited highly bifunctional activity for alkaline water electrolysis. Thus, the hierarchical 3D heterostructure serves as an ideal model for constructing high-performance, bifunctional electrode materials for alkaline OWS application.

3.2. Structural and morphological characterization

3.2.1. Characterization of MnCo-LDH/NF, NiS–Ni_3S_2/NF, and MnCo-LDH@NiS–Ni_3S_2/NF

The surface morphology, microstructural features, and elemental composition of the as-prepared electrode materials were investigated using a field-emission scanning electron microscope (FE-SEM) and energy-dispersive X-ray spectroscopy (EDX). The FE-SEM and EDX images of MCNS/NF, MnCo-LDH/NF, and NiS–Ni_3S_2/NF are shown in Fig. 2 & Figs. S3–S6. MnCo-LDH/NF exhibited uniform growth and a cross-linked, flexible nanosheet structure with vertically oriented hollow channels covering the NF substrate after the hydrothermal reaction. The magnified FE-SEM images revealed the cross-linked nanosheet structure offering a rich array of electrochemically active sites. It facilitated the construction of efficient transport channels for electrolyte accessibility and charge transfer during electrochemical reactions, consequently propelling further improvement in electrochemical performance. Furthermore, as shown in Fig. S4, the EDX and corresponding elemental mapping results from FE-SEM image analysis clearly illustrated the uniform distribution of Mn, Co, Ni, C, and O elements throughout the nanosheet arrays with a stoichiometric composition of 5.71, 3.75, 38.68, 14.91 and 36.95%, respectively, making honeycomb-like MnCo-LDH/NF nanosheets an ideal template for the growth of various redox-active materials and validating the co-precipitation pathway proposed in Equations (1)–(10).

Fig. S5 displays FE-SEM images of hierarchical nanoflowers, including NiS–Ni_3S_2/NF nanoarrays. NiS–Ni_3S_2/NF nanoflowers possess a 3D network structure grown on the entire surface of the NF skeleton, with a greater number of mesoporous channels. Moreover, the higher-magnification FE-SEM images revealed that these nanoflowers had an average diameter of 3 μm and relatively smooth surfaces. This feature not only provided an abundant reaction-active center to accelerate electrolyte contact but also facilitated gas release, thereby improving the electrocatalyst's efficiency. Additionally, Fig. S6 shows the EDX spectra of NiS–Ni_3S_2/NF nanoarrays, confirming the existence of Ni, S, and O. Furthermore, the EDX mapping image of NiS–Ni_3S_2/NF nanoarrays showed a homogeneous spatial distribution of Ni, S, and O throughout the nanoflower structure, corresponding to atomic concentrations of 55.03, 4.25, and 40.72%, respectively, supporting the sulfidation pathway described in Equations (11)–(16).

Moreover, Fig. 2a–f displays the FE-SEM images of hybrid heterogeneous MCNS/NF nanoarrays at different magnifications, revealing uniform and dense growth on the surface of 3D open nanoporous NF. The low-magnification images showed that the NiS–Ni_3S_2 nanoarrays were uniformly anchored to the MnCo-LDH nanosheet architecture, which consisted of 3D nanoflakes with an average nano-flower diameter of 14 μm. The high-magnification FE-SEM image revealed that the average diameter of the formed nanoparticles was 425-530 nm. Hence, this 3D hierarchical heterostructure composed of nanosheets arranged in a flower-like porous heterostructure is expected to function as an optimal scaffold. Its expanded surface area and interconnected metal oxo-hydroxide and metal-sulfide networks facilitated efficient electron and ion transport throughout the electrocatalytic process. Additionally, elemental distribution of the hetero-nanostructure was further confirmed by EDX and corresponding mapping analysis (Fig. 2g-m). The EDX elemental mappings of homogeneously dispersed Mn, Co, Ni, S, and O elements indirectly confirmed the presence of MnCo-LDH nanosheets and NiS–Ni_3S_2 nanoarrays phases in the hybrid MCNS/NF heterostructure with an average stoichiometric proportion of 3.11, 1.18, 50.39, 6.17, and 39.15%, respectively. According to the overall outcomes, it was confirmed that NiS–Ni_3S_2 nanoarrays were successfully constructed on the surface of the MnCo-LDH/NF nanosheets without aggregation, which is in good agreement with the proposed reaction pathway (Equations (1)–(16)), suggesting that the MnCo-LDH/NF nanosheets phases can provide more nucleation sites for the growth of surrounding NiS–Ni_3S_2 nanoarrays during the hydrothermal process.

The accurate crystallographic structures and phase purity of the as-prepared electrode materials were examined by powder X-ray diffraction (PXRD). As shown in Fig.3 and S7, both electrode materials displayed prominent and sharp diffraction peaks at $2\theta \approx 44.6$, 51.8, and 76.5° corresponding to the peaks of (111), (200), and (220) crystalline planes of face-center cubic Ni of the NF substrate (JCPDS, card No. 04-0850), denoted by the symbol (Ψ), respectively. The characteristic peaks at $2\theta \approx 9.81$, 24.44, 32.25, 33.32, 38.09, 41.98, 45.89, 59.53, and 61.05° in Fig. S7a, could be well ascribed to (003), (006), (012), (009), (015), (107), (018), (110), and (113) facets, which confirmed the formation of typical 2D MnCo-LDH phase corresponding to Equation (10), and are marked with the symbol (◆), which was compatible with the previous study [46]. As illustrated in Fig. S7b and S7c, the well-defined diffraction peaks at $2\theta \sim 21.89$, 30.79, 37.46, 38.27, 44.33, 49.79, 54.65, 55.45, 68.80, 72.44, and 77.09° can be indexed to (101), (012), (003), (021), (202), (113), (300), (104), (131), (214), and (401) planes of rhombohedral structural heazlewoodite Ni_3S_2 phases (JCPDS, card No. 08-0126), denoted by (♥), while the peaks at $2\theta \approx 30.82$, 32.23, 35.67, 37.68, 40.52, 49.82, 52.45, 55.69, 57.30, and 59.53° can be assigned to (101), (300), (021), (220), (211), (410), (401), (321), (330), and (012) planes of the standard phase of rhombohedral structural millerite NiS composition (JCPDS, card No. 12 0041), marked with (♠), revealing the formation of hierarchical nanoflower-like NiS–Ni_3S_2/NF, predicted in Equations 15 and 16, is a hybrid of Ni_3S_2 and NiS. Moreover, as shown in Fig. 3a–c, the XRD pattern of the multi-metallic MCNS/NF heterostructure demonstrated that the diffraction peak intensity became consistently more distinct and well aligned with MnCo-LDH nanosheets and NiS–Ni_3S_2 nanoarrays. Among these, the peak intensity of NiS–Ni_3S_2 nanoflower shell-phases was more pronounced compared to MnCo-LDH nanosheet phases, confirming that the dense nanosheet arrays were tightly wrapped by the shell-nanoflower arrays with no emergence of Mn–S or Co–S bulk sulfide phases and also implying excellent surface growth with effective interparticle interaction on the surface of the NF substrate and a better-defined crystal structure without impurities (Equations (1)–(16)).

Fourier Transform Infrared (FT-IR) spectroscopy was employed to examine the functional groups of the electrocatalysts and detect spectroscopic changes in their internal chemical bonding. Fig. 3d, and Fig. S8a and S8b represent the FT-IR spectra of MCNS/NF, MnCo-LDH/NF, and NiS–Ni_3S_2/NF nanoarrays. For the MnCo-LDH/NF nanosheet array, the broad absorption band at 3150-3650 cm^{-1} can be attributed to the stretching and bending vibrations of intercalated water molecules and metal-bonded –OH groups [47]. Additionally, it can be observed that the existence of a weaker band at 1680 cm^{-1} is accompanied by the –OH bending vibration of the trapped hydroxyl and water molecules of the LDH layers. The peaks at 1372-1550 and 830 cm^{-1} belonged to the stretching vibration of the asymmetric and symmetric modes of

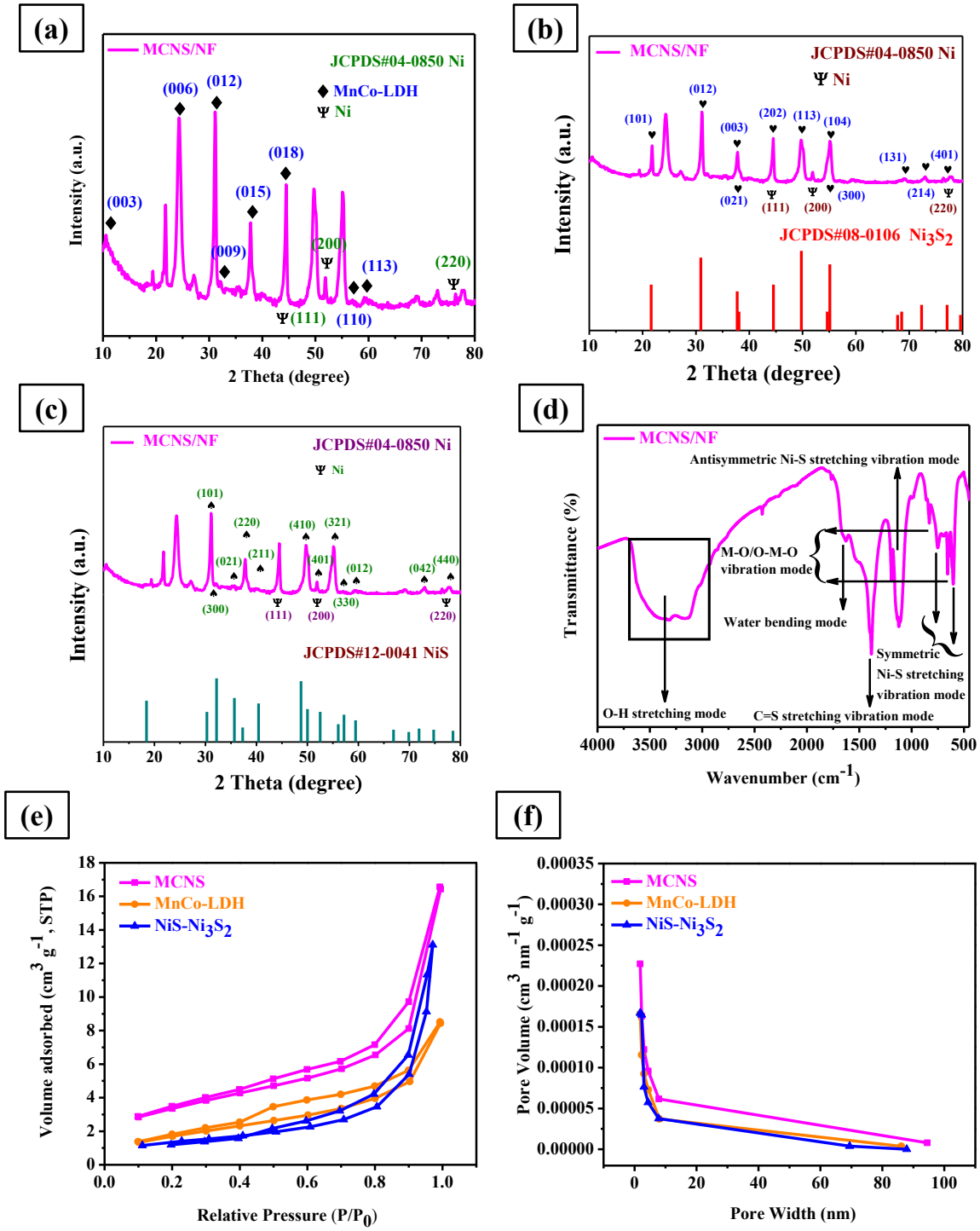

Fig. 3. High magnification PXRD pattern (a-c); typical FT-IR spectrum of MCNS/NF heterostructure. electrocatalyst (d); N_2 adsorption-desorption isotherm curves and typical BJH pore size distribution model of MnCo-LDH, NiS–Ni_3S_2, & MCNS materials (e & f).

interlayer carbonate ions, which can be attributed to the decomposition of urea in the precursor solution [48]. The shoulder peak at 1160-1190 cm^{-1} corresponds to the C–O stretching vibration mode of CO_3^{2-} species. The appearance of the sharp absorption peaks at 585, 654, and 746 cm^{-1} was attributed to the stretching vibration modes of O-*M*-O and M − O bonds, where M = Mn and Co. The FT-IR spectra of hierarchical nanoflower-like NiS–Ni_3S_2/NF nanoarrays disclosed the well-defined absorption peaks at 3100-3650 and 1635 cm^{-1}, which are attributed to the stretching and bending vibration mode of the corresponding –OH groups of the surface-adsorbed water molecules. Furthermore, the strong characteristic peaks at 2000-2250 cm^{-1} may be attributed to intramolecular hydrogen bonding between water molecules. Additionally, the observed peaks at 755, 595, and 1115 cm^{-1} corresponded to the symmetric and asymmetric stretching vibration modes of Ni–S bonds [49]. The presence of additional peaks at 1405 and 665 cm^{-1} in the spectrum of NiS–Ni_3S_2/NF nanoarrays can be attributed

to the C=S and O-*M*-O (M = Ni) vibration modes. The FT-IR spectrum of MCNS/NF disclosed the peaks at 3100-3650 and 1660 cm^{-1}, which can be attributed to the –OH stretching mode of hydrogen-bonded hydroxyl groups, and the bending vibration mode of the intramolecular hydrogen-bonded adsorbed –OH of the metal surface [50]. The significant divergence in the broad –OH band range was attributed to the hydrogen bonding, implying that MCNS/NF was hygroscopic. In addition, the peaks observed at 1390, 1130, 757, and 580 cm^{-1} were attributed to the C=S stretching, as well as the symmetric and asymmetric stretching vibration modes of the Ni–S bond [51]. This partial sulfurization was further reflected in the increased intensity of the distinct functional groups, indicating efficient interaction between the nanosheet phase and the nanoflower array, thereby significantly facilitating the transfer of ions and electrons. Furthermore, the peaks that appeared at 650 and 845 cm^{-1} were generally due to the vibration mode of M − O or O-*M*-O (M = Mn/Co/Ni) groups, and were highly intense compared to MnCo-LDH/NF nanosheets and NiS–Ni_3S_2/NF nanoflowers array, indicating the successful formation of 3D MCNS/NF heterostructure [52]. BET surface area analysis revealed that the MnCo-LDH@NiS–Ni_3S_2 heterostructure exhibited a surface area of 11.87 $m^2\ g^{-1}$, which is higher than that of MnCo-LDH (6.54 $m^2\ g^{-1}$) and NiS–Ni_3S_2 (5.30 $m^2\ g^{-1}$). Similarly, the total pore volume increased to 0.021 $cm^3\ g^{-1}$ for MnCo-LDH@NiS–Ni_3S_2 compared with 0.012 and 0.011 $cm^3\ g^{-1}$ for MnCo-LDH and NiS–Ni_3S_2, respectively (Fig. 3e & f). This increase indicates the formation of additional interfacial voids within the heterostructure. Consequently, the optimized pore framework provided more accessible electroactive sites, facilitating efficient electrolyte penetration and ion transport, thereby contributing to the observed improvements in electrocatalytic activity.

Moreover, the in-depth microstructural analysis, such as surface morphology, lattice spacing, crystal defect, heterointerface, and atomic distribution over the as-prepared electrocatalyst, was further investigated by transmission electron microscopy (TEM), high-resolution TEM (HR-TEM), selected area electron diffraction (SAED), energy dispersive spectrometer (EDS), and high-angle annular dark-field scanning transmission electron microscopy (HAADF-STEM). As shown in Fig. S9a–e, the TEM and HR-TEM images of MnCo-LDH/NF exhibited an irregular transparent nanosheet-like morphology. HR-TEM and Fast Fourier Transform (FFT) image analysis displayed the existence of uniform lattice fringes with the interplanar distances of 0.233, 0.275, 0.214, 0.197, and 0.151 nm, which coincide with the interlayer spacing of the (015), (012), (107), (018), and (113) planes of the MnCo-LDH/NF (Fig. S9f–j). The well-defined SAED pattern image further revealed that the hexagonal polycrystalline nanosheet-like MnCo-LDH/NF arrays consisted of five relatively bright diffraction rings indexing to the (015), (018), (012), (113), and (107) facets, respectively (Fig. S10a). To further substantiate the polycrystalline nature of the MnCo-LDH/NF nanosheet arrays, the SAED pattern was quantitatively analyzed by extracting the corresponding azimuthally integrated intensity line profile. The resulting intensity distribution exhibited multiple diffraction peaks, a characteristic of polycrystalline domains composed of randomly oriented nanoscale crystallites, confirming their defect-rich nature (Fig. S10b). Each diffraction maximum in the intensity profile can be reliably indexed to the (012), (107), (018), and (113) crystallographic planes of the hexagonal MnCo-LDH, in excellent agreement with the interplanar spacings measured from the HR-TEM lattice fringes and the corresponding FFT analyses. Moreover, the HR-TEM-EDS and the associated HAADF-STEM elemental mapping images validated the uniform distribution of Mn, Co, Ni, O, and C in the whole MnCo-LDH/NF in Fig. S10c–j, which supports the above-mentioned urea-assisted hydrolysis and co-precipitation reactions described in Equations (1)–(10). Thus, this defect-rich nanosheet configuration provided a high electrochemically active surface area with abundant active sites, facilitating fast electron transport and improving ion penetration across the electrode surface. These features are advantageous for electrochemical water splitting applications. As shown in Fig. S11a–d, the TEM and HR-TEM images of the synthesized NiS–Ni_3S_2/NF nanoflower arrays revealed a nano-petal-like structure, in which nanoflowers were composed. The HR-TEM image and IFFT patterns of the selected zone in Figures S11e & S12a-f showed distinct strips with interplanar spacings of 0.275, 0.294, and 0.224 nm, corresponding to the (300), (101), and (211) planes of the hexagonal NiS phase. In addition, the lattice fringes with an interplanar spacing of 0.238, 0.181, and 0.209 nm, which coincided with the (003), (113), and (202) crystal planes of the hexagonal polycrystalline Ni_3S_2 phase, demonstrated that the NiS–Ni_3S_2/NF nanoflower arrays consisted of the heterojunction between the neighbouring region of NiS and Ni_3S_2. Furthermore, the lattice fringe analysis shown in Fig. S12g revealed a heterointerface between the NiS and Ni_3S_2 phases, marked by a dotted line, visually validating the subsequent thiourea-assisted sulfidation mechanism (Equations (11)–(16)) for the formation of a hybrid heterostructure. Thus, the co-existence of distinct grain boundaries between the NiS and Ni_3S_2 phases and these coarser defect surfaces not only optimized the adsorption energy of the electrocatalyst through interface electronic coupling, but also provided additional charge transfer pathways to the altered surface electronic structure, drastically reducing charge transfer resistance and boosting electron transport ability, which in turn improved the electrochemical performance. Furthermore, the SAED pattern of the hybrid NiS–Ni_3S_2/NF nanoflower arrays shown in Figure S12h confirmed that the green dashed lines correspond to the (211), (021), and (012) crystal planes of NiS, while the yellow dashed lines represent diffraction rings indexed to the (321), (241), and (502) lattice planes of the Ni_3S_2 phase. To further corroborate the crystallographic nature of the NiS–Ni_3S_2 nanoarrays, the obtained radial diffraction intensity line profile displayed a series of continuous diffraction maxima instead of discrete diffraction spots, which is a characteristic feature of polycrystalline materials consisting of randomly aligned nano-crystallites (Fig. S13a). The diffraction maxima extracted from the intensity profile can be unambiguously indexed to the characteristic crystallographic planes of the NiS–Ni_3S_2 phase, specifically the (021), (211), and (012) planes of hexagonal NiS, along with the (241) and (502) planes of the hexagonal Ni_3S_2, which reflected the presence of defect-rich grain boundaries in the heterophase structure. These assignments are fully consistent with the interplanar spacings derived from HR-TEM images, FFT analyses, and XRD results. In addition, HAADF-STEM-EDS also confirmed the homogeneous spatial distribution of Ni, S, and O elements throughout the 3D-hybrid nanoflower arrays, which provided sufficient active centers to speed up the electrochemical activity (Fig. S13b–g). Fig. S14a–d displays the TEM image of hierarchical marigold flower-like heterogeneous MCNS/NF nanoarrays. The HR-TEM images of the heterostructure are shown in Fig. 4a & b, suggesting the hierarchical, few-layered NiS–Ni_3S_2 nanopetals grown on thin, single-layered hexagonal MnCo-LDH nanosheets, confirming the formation of a multi-metallic heterogeneous nanostructured electrocatalyst. Despite this, the HR-TEM image with 5 nm resolution revealed periodic crystalline lattice fringes in a specific orientation. The FFT patterns showed that the measured d-spacing value of 0.218 and 0.239 nm unambiguously corresponded to the (107) and (015) facets of the MnCo-LDH phase, respectively (Fig. 4c & d). Moreover, the lattice spacing of 0.221 and 0.247 nm is associated with the (211) and (220) planes of NiS (Fig. 4e & f). On the contrary, the layered spacing of 0.230 and 0.213 nm in the outer region corresponds to the (021) and (202) crystal planes of Ni_3S_2, respectively (Fig. 4g & h). In Fig. 4i–a clear grain boundary was observed between the MnCo-LDH, Ni_3S_2, and NiS phases. In addition, the bright part corresponded to the MnCo-LDH nanosheets in the inner region, while the relatively dark part was confined to the outer region, which corresponded to the Ni_3S_2 and NiS phases due to overlapping growth between the MnCo-LDH and the Ni_3S_2 and NiS nanoflower arrays, thereby revealing the multicomponent heterostructure. HR-TEM image analysis suggested that the nanoflower arrays anchoring on the nanosheet's surface possessed abundant defects and disorder, which contribute to tailoring numerous intimate sites for catalyzing the water electrolysis process. Additionally,

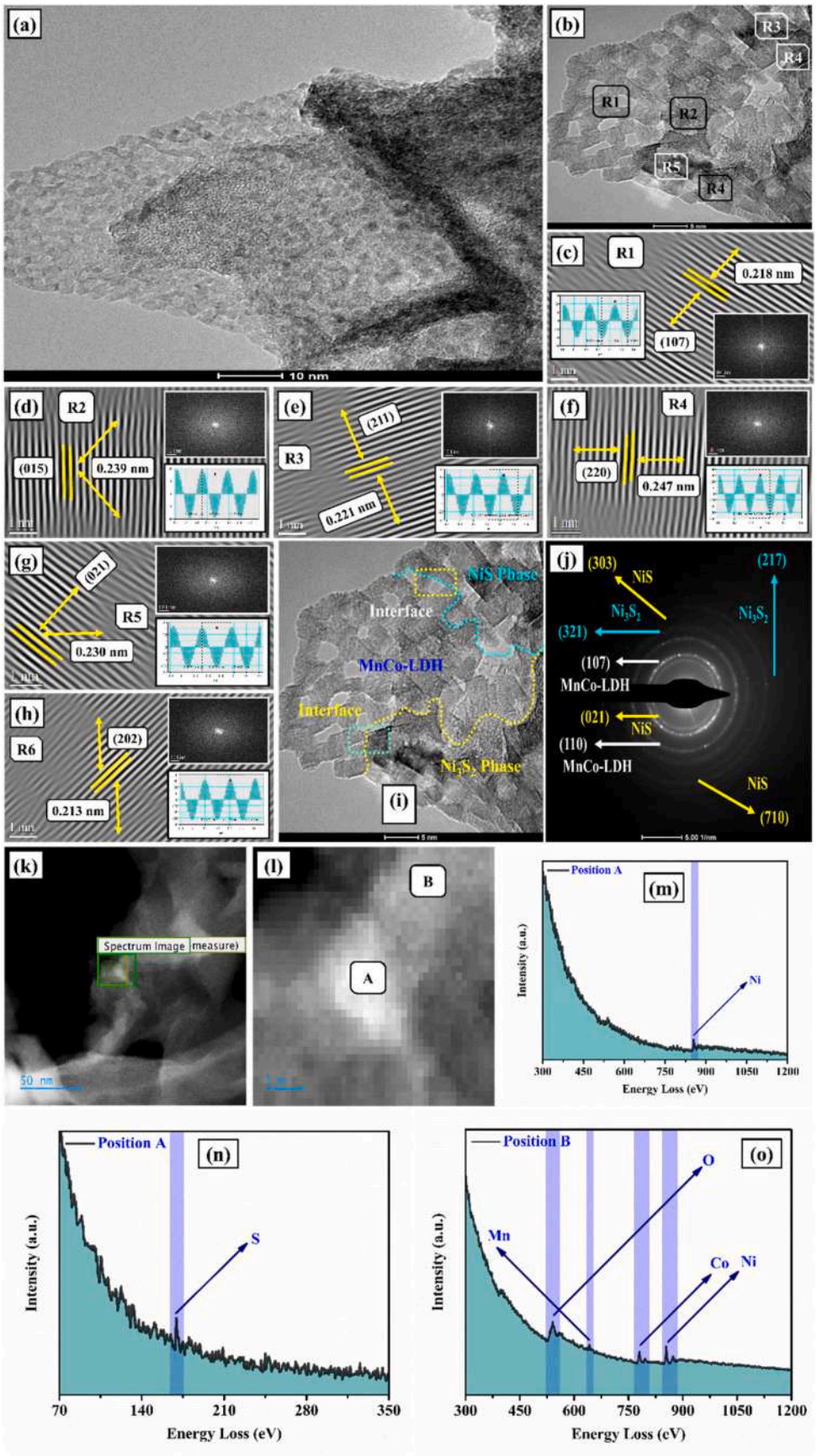

Fig. 4. HR-TEM images of the MCNS/NF heterostructure electrocatalyst (a & b); IFFT patterns of the lattice fringes along with lattice d-spacing of the co-existing phases of the selected region of HR-TEM (c & h); heterojunction (i); SAED pattern (j); AC-HAADF-STEM (k & l); and STEM-EELS point spectrum of the selected region (m-o).

the SAED pattern image shown in Fig. 4j revealed a set of bright rings, attributed to the characteristic (107), and (110) planes of MnCo-LDH poly-crystalline phase, along with the (303), (021), and (710) planes of anchored NiS and (321), and (217) planes of Ni_3S_2 phases, respectively. Moreover, the radial diffraction line profile displayed multiple continuous and broadened diffraction maxima, which is an inherent characteristic of a polycrystalline structure comprised of randomly synchronised nanoscale crystallites, confirming the presence of abundant heterointerfaces coupled with lattice defects and grain boundaries, consistent with the defect-rich nature of both inner and outer components (Fig. S14e). The diffraction peaks in the line pattern might be reliably indexed to the distinctive planes of the heterostructure, whereas (107) and (110) planes of the MnCo-LDH phase, and (021), (241), (321), (303), and (710) planes corresponding to the NiS–Ni_3S_2 phase. These outcomes are highly consistent with HR-TEM lattice fringe measurements, FFT estimation, and XRD data. In addition, the TEM-EDS and HAADF-STEM spectra of the MCNS/NF heterostructure, in Fig. S15a–h, illustrated that Mn, Co, and O signals were concentrated in the core, whereas Ni and S elements were predominantly distributed in the outer phase in the nanoflower structure and minimal incorporation within the LDH inner phase. These results provided compelling evidence for a heterostructure rather than complete sulfuration. Furthermore, aberration-corrected high-angle annular dark-field scanning transmission electron microscopy (AC-HAADF-STEM) together with spatially resolved along with electron energy loss spectroscopy (EELS) analysis clearly demonstrated the co-existence of MnCo-LDH and NiS–Ni_3S_2 phases within the multi-component heterostructure, along with the abundant heterointerface (Fig. 4k-o). These overall findings were well aligned with the XRD and FE-SEM results. Thus, the above findings further confirmed the formation of MCNS hybrid nanoflower arrays on the surface of NF, with artistic hetero-nanostructures.

A deeper understanding of the accurate chemical composition, surface valence states, coordination environments, and surface electronic interactions of the prepared electrocatalysts was obtained by using surface X-ray photoelectron spectroscopy (XPS). XPS measurements were performed with binding-energy calibration and charge correction applied, using the adventitious carbon C 1s peak at 284.8 eV as an internal reference. As shown in Figs. S16a, S16b, and 5a, the XPS survey spectrum of the resultant electrocatalysts corroborated the occurrence of Mn, Co, C, and O elements in MnCo-LDH/NF, Ni, S, and O elements in NiS–Ni_3S_2/NF, and Mn, Co, Ni, S, and O elements in MCNS/NF, without any additional impurities (Tables S2–S4). These outcomes correspond to the FE-SEM-EDX, XRD, and HR-TEM-EDS results. As shown in Fig. 5b, the high-resolution XPS spectra of Mn 2p in the MCNS/NF contained a

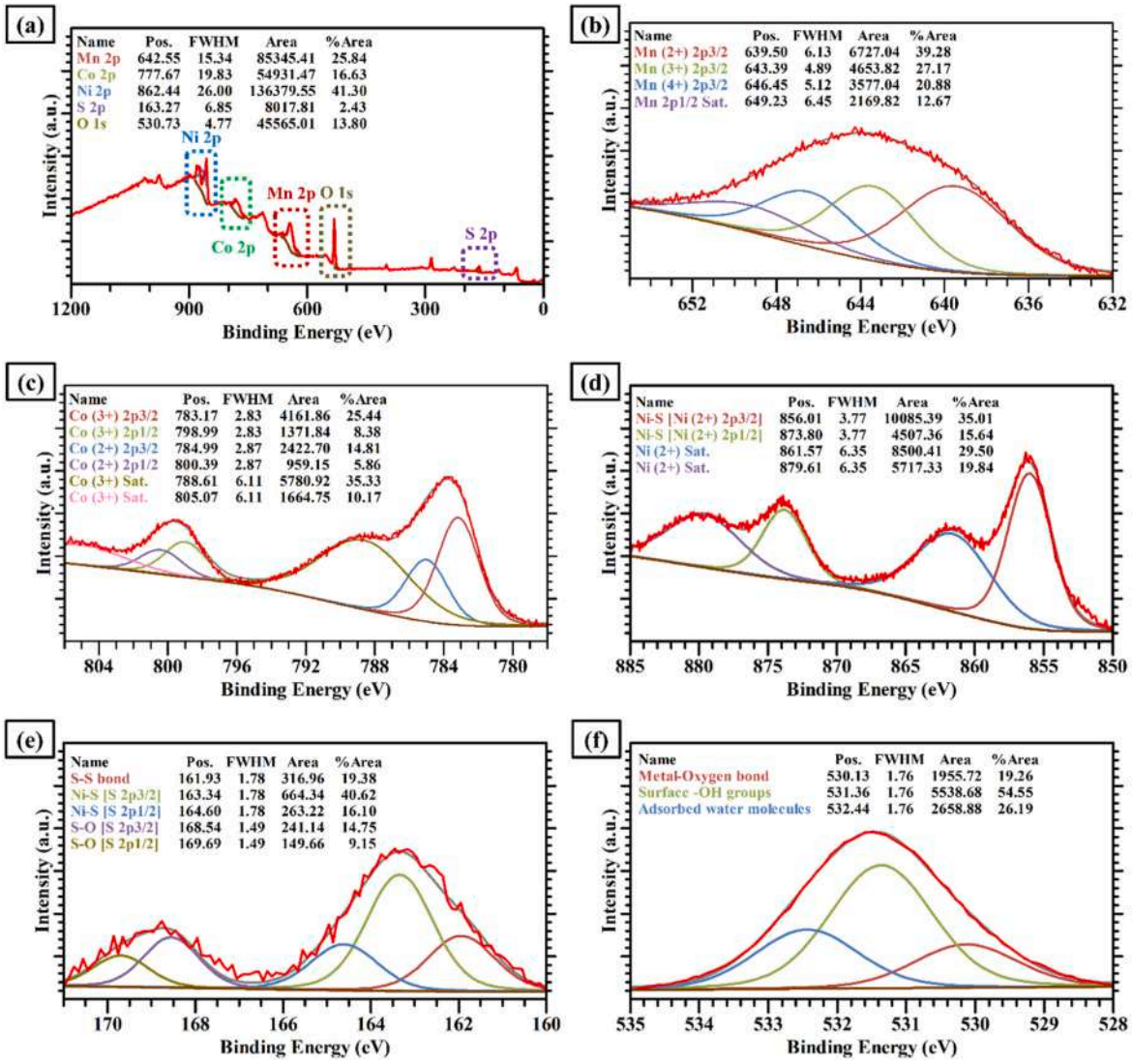

Fig. 5. High-resolution XPS survey spectra (a); deconvoluted core-level XPS spectra for binding energies of Mn 2p (b); Co 2p (c); Ni 2p (d); S 2p (e); & O 1s (f) for MCNS/NF heterostructure electrocatalyst.

peak at 639.50 eV, analogous to the Mn^{2+}. The other three well-resolved peaks at 643.39, 646.45, and 649.23 eV can be attributed to Mn^{3+}, Mn^{4+}, and the shake-up satellite of Mn 2p1/2 (donated as "sat."), respectively. A plausible reason for the existence of the Mn^{4+} state was ascribed to the lower oxidation potential and inferior chemical stability of the Mn^{3+} state [53]. The XPS spectra of Mn 2p confirmed the existence of the Mn^{2+} and Mn^{3+} states in the form of metal hydroxide in the MnCo-LDH phase without the appearance of Mn–S related peaks, which indicated the MnCo-LDH framework is chemically stable under the applied sulfuration conditions [54]. In contrast, for the MnCo-LDH/NF, the analogous peaks of MCNS/NF shifted positively, and an increased peak area ratio, suggesting a change in the electronic environment of the Mn to facilitate the formation of higher valent Mn ions, through transfer of electrons from Mn to Co and strong electronic interaction on the heterointerface (Fig. S17, Table S5 & Table S7). Therefore, the higher-valent Mn ions at the interface act as an electronic buffer, facilitating OH^- adsorption and deprotonation kinetics and contributing dominantly to the multi-electron OER process. Fig. 5c reveals the deconvoluted core-level XPS spectrum of Co 2p in MCNS/NF, showing the occurrence of two predominant peaks at 783.17 and 798.99 eV, corresponding to the Co^{3+}. In addition, the low-intensity fitting peaks at 784.99 and 800.39 eV can be attributed to Co^{2+}. Similarly, a pair of accompanied shake-up satellites located at 788.61 and 805.07 eV (donated as "sat."), confirmed the coexistence of cobalt ions in both trivalent and divalent forms within the MCNS/NF heterostructure [55]. More notably, compared with the MnCo-LDH/NF, the Co 2p peak position of MCNS/NF exhibited a notable shift towards higher binding energy, implying that the MnCo-LDH phase acts as an "electron donor" as well as the complete absence of such low-binding energy Co–S signatures implies that Co present in the MnCo-LDH lattice does not undergo bulk sulfuration (Tables S5 and S7). Furthermore, higher-valent Co ions facilitated the formation of an active oxyhydroxide phase at the interface, thereby reducing the OER overpotential. Therefore, it is noteworthy that there is a certain interface region at the junction of MnCo-LDH and NiS–Ni_3S_2 phases, where a greater number of electrons are transferred through the MnCo-LDH to the NiS–Ni_3S_2 phase. This existence will modulate the electronic structure of atoms in the interface region, ultimately improving electronic conductivity and enhancing electrocatalytic activity. As shown in Fig. 5d, the high-resolution XPS spectra of Ni2p in MCNS/NF heterogeneous nanoarrays showed the spin-orbit splitting into two major peaks positioned at 856.01 and 873.80 eV, typically associated with the Ni^{2+} of the Ni–S bond. Meanwhile, the other set of peaks appeared at 861.57 and 897.61 eV, accompanied by two shake-up satellites that can be uniquely ascribed to Ni 2p1/2 and Ni 2p1/2 of the Ni–S bond [56]. Notably, the binding energy corresponding to the Ni 2p in MCNS/NF had a positive shift, contrary to the pristine NiS–Ni_3S_2/NF electrocatalyst (Fig.S18, Table S6, & Table S7). Thus, the above outcomes revealed a favourable transfer of binding energy from Ni to the NiS–Ni_3S_2 phase, indicating that the electrons accumulated at the MnCo-LDH region and were depleted at the electron-acceptor NiS–Ni_3S_2 region. Therefore, Ni ions in the Ni–S bond are expected to serve as the primary active site for HER, facilitating proton adsorption and subsequent hydrogen evolution. Such redistribution of electrons between the two constituents may promote efficient charge transport at the interface, thereby modulating the energy of reaction intermediates to enhance their reactivity in the multi-component architecture. The S 2p spectra shown in Fig. 5e can be deconvoluted into two visible peaks centered at 163.34 and 164.60 eV, corresponding to the S 2p3/2 and S 2p1/2, manifesting the signals of the Ni–S bond. In addition, the other doublet of S 2p3/2 and S 2p1/2 at 168.54 and 169.69 eV was associated with the S–O bond that can be indexed to the oxidized S species on the surface because of the aerial oxidation. Note that the peak at 161.93 eV can be assigned to the S–S bond, manifesting the existence of a well-anchored S element on the surface of the NiS–Ni_3S_2 phase. Meanwhile, compared with hierarchical nanoflower-like NiS–Ni_3S_2/NF, the S 2p binding energy showed a large positive shift (Tables S6 and S7). Surprisingly, the above result indicates that incorporating the MnCo-LDH phase can regulate the surface electronic configuration of the NiS–Ni_3S_2 phase, potentially increasing the oxidation state of Ni/S ions and strengthening interactions of reactants and/or intermediates with the catalyst surface, thereby improving electrocatalytic activity in an alkaline medium. On the other hand, as presented in Fig. 5f, the XPS spectrum of O 1s is due to the inevitable surface oxidation in the MCNS/NF heterogeneous nanoflower and was deconvoluted into three peaks at 530.13, 531.36, and 532.44 eV, which were characterized as metal-oxygen bond, surface –OH groups, and adsorbed water molecules, respectively. The heterostructure exhibited nearly identical O 1s spectra compared to the remaining electrocatalysts, except for a noticeable positive shift in the metal-oxygen bond, affirming the existence of higher lattice oxygen-content species on the heterointerface and superior encapsulation capabilities, which substantially improved the electron interactivity with reaction intermediates. Moreover, in Fig. S17, the narrow scan spectra of the C 1s signal can be deconvoluted into five surface carbon components at 283.64, 284.91, 286.18, 288.37, and 289.79 eV, which are associated with the C–C, C-(H), C=, O-C=O, and pi-pi species. The detected peaks in the C 1s spectra attributed to their constituent components further provided evidence of the successful formation of the MnCo-LDH nanosheet arrays. According to the above XPS analysis, the presence of the MnCo-LDH phase influenced the formation of the NiS–Ni_3S_2 phase in the hierarchical MCNS/NF heterostructure.

Additionally, AC-HAADF-STEM combined with EDS line-scan analysis was performed to probe the spatial elemental distribution and the presence of a heterointerface across the MCNS/NF heterostructure (Fig. 6a–i). The AC-HAADF-STEM image clearly revealed a well-defined heterostructure architecture with a distinct boundary area between the inner MnCo-LDH and the outer NiS–Ni_3S_2 phases. The corresponding line-scan spectrum showed that Ni and S signals were strictly confined to the outer region, while Mn, Co, and O were predominantly localized within the core. This architecture enabled boosted reaction kinetics for the incorporation of metal-oxyhydroxide and metal-sulfur phases within the interior or at the surface. Furthermore, the multiple defect states and numerous heterointerfaces could contribute to the electrical conductivity of the NiS–Ni_3S_2 phase and deliver electrons to the MnCo-LDH phase through the close contact of the as-fabricated electrocatalyst. Thus, these features make the hetero-nanostructure a promising, highly efficient electrocatalyst for alkaline OWS.

3.3. Electrocatalytic activity evolution for alkaline water electrolysis

3.3.1. Alkaline HER performances

The HER catalytic activities of the developed electrocatalysts were measured using a standard three-electrode (conventional electrode) setup in 1.0 M KOH at room temperature. As shown in Fig. S19, the schematic depicts the possible HER mechanism in an alkaline environment. Fig. 7a shows the 100% iR-corrected linear sweep voltammogram (LSV) of the as-prepared electrocatalysts compared with state-of-the-art 20 wt% Pt/C, measured at a scan rate of 5.0 mV s^{-1} to evaluate their intrinsic electrocatalytic activity. To achieve a current density of 10 mA cm^{-2}, MCNS/NF exhibited a small overpotential (η) value of 83 mV, which, although higher than that of 20% Pt/C/NF (29 mV) remains significantly lower to its other counterparts, specifically, NiS–Ni_3S_2/NF (132 mV), MnCo-LDH/NF (195 mV), and bare NF (204 mV), respectively (Table S8). Additionally, at a current density of 10 mA cm^{-2}, the η histogram showed comparable performance between MCNS/NF and other electrocatalysts (Fig. 7b). The exceptionally low η of the MCNS/NF heterostructure was attributed to the combined effect of MnCo-LDH and NiS–Ni_3S_2 phases. Furthermore, the intrinsic electrocatalytic activity and the reaction kinetics of the as-prepared electrode materials can be verified using the Tafel slope. As shown in Fig. 7c, the MCNS/NF electrocatalyst revealed the smallest Tafel slope value of 52 mV dec^{-1}, close to that of 20% Pt/C/NF (36 mV dec^{-1}) and

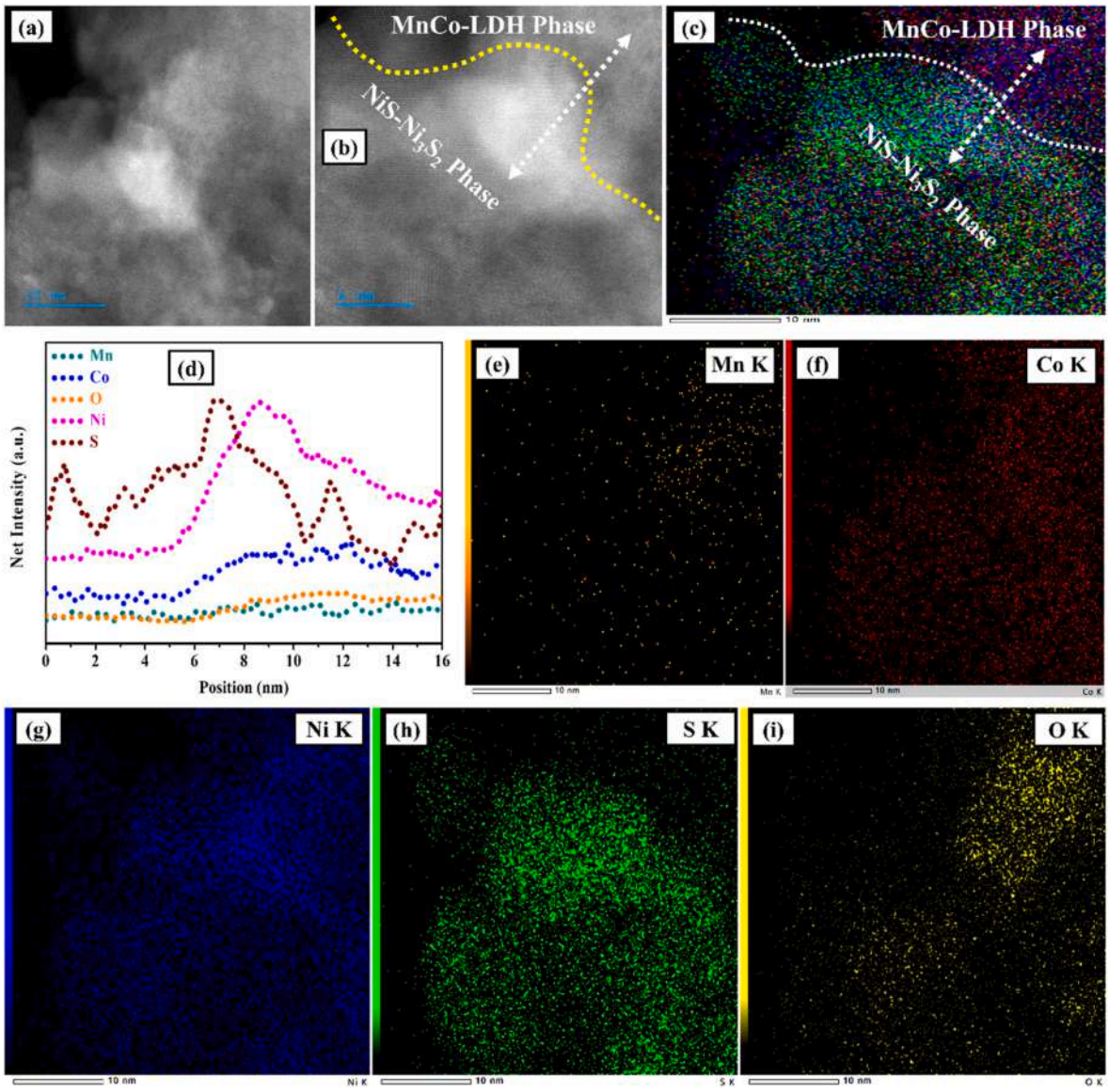

Fig. 6. AC-HAADF-STEM image (a & b); the Overlay EDS elemental mapping (c); line-scan spectrum (d); and the corresponding EDS elemental mapping of individual elements (e-i) for MCNS/NF heterostructure electrocatalyst.

significantly lower than those of NiS–Ni_3S_2/NF (63 mV dec^{-1}), MnCo-LDH/NF (75 mV dec^{-1}), and bare NF (85 mV dec^{-1}) (Table S8). The outstanding HER cathodic process on the surface of the MCNS/NF heterostructure electrocatalyst followed the Volmer-Heyrovsky mechanism, with the Heyrovsky step as the rate-determining step (RDS) in the overall reaction pathway. This indicates that after the initial water dissociation and hydrogen adsorption, the subsequent electron-transfer-coupled hydrogen desorption governed the overall reaction rate. This suggests that the MCNS/NF electrocatalyst effectively facilitated water dissociation and promoted efficient electrochemical hydrogen desorption. Additionally, the charge-transfer coefficient (α), derived from the Tafel slopes, further supported the accelerated HER kinetics of the electrocatalysts. The calculated α values followed the order 20% Pt/C/NF (1.64) > MCNS/NF (1.14) > NiS–Ni_3S_2/NF (0.94) > MnCo-LDH/NF (0.79) > bare NF (0.70), indicating progressively improved electron-transfer efficiency. In particular, the relatively high α value of MCNS/NF (1.14) reflects rapid charge transfer and more favourable electron-transfer behavior for the rate-determining Heyrovsky step (Table S8). This observation confirmed that the heterostructure effectively facilitated electron-transfer-coupled hydrogen desorption, thereby enhancing overall HER kinetics. In addition, to further examine the interfacial charge-transfer mechanism, the charge-transfer resistance (R_{ct}) at the electrode-electrolyte interface and the internal resistance of the electrochemical system were evaluated by electrochemical impedance spectroscopy (EIS). After the EIS study, the fitted Nyquist plot and corresponding equivalent circuit model were proposed to identify the R_{ct} of the prepared electrocatalyst (Fig. 7d, & Table S9). The semicircle of MCNS/NF was consistent with the R_{ct} of only 6.30 Ω, which was higher than that of the 20% Pt/C/NF (3.19 Ω), yet significantly lower than those of NiS–Ni_3S_2/NF (11.48 Ω), and of the other comparatives of MnCo-LDH/NF (21.80 Ω), and bare NF (34.90 Ω), respectively. The significantly lower R_{ct} of MCNS/NF demonstrated rapid electronic transmission at the heterointerface in the hierarchical multi-component MCNS and the alkaline electrolyte, thereby promoting reaction kinetics and enhancing HER electrochemical performance. Furthermore, the electrochemically active surface area (ECSA) was considered a powerful indicator of the electrochemically active sites, which are highly responsible for the electrocatalyst's intrinsic electrocatalytic activity. The ECSA of 20% Pt/C/NF, MCNS/NF, NiS–Ni_3S_2/NF, MnCo-LDH/NF, and bare NF were obtained from the electrochemical double layer

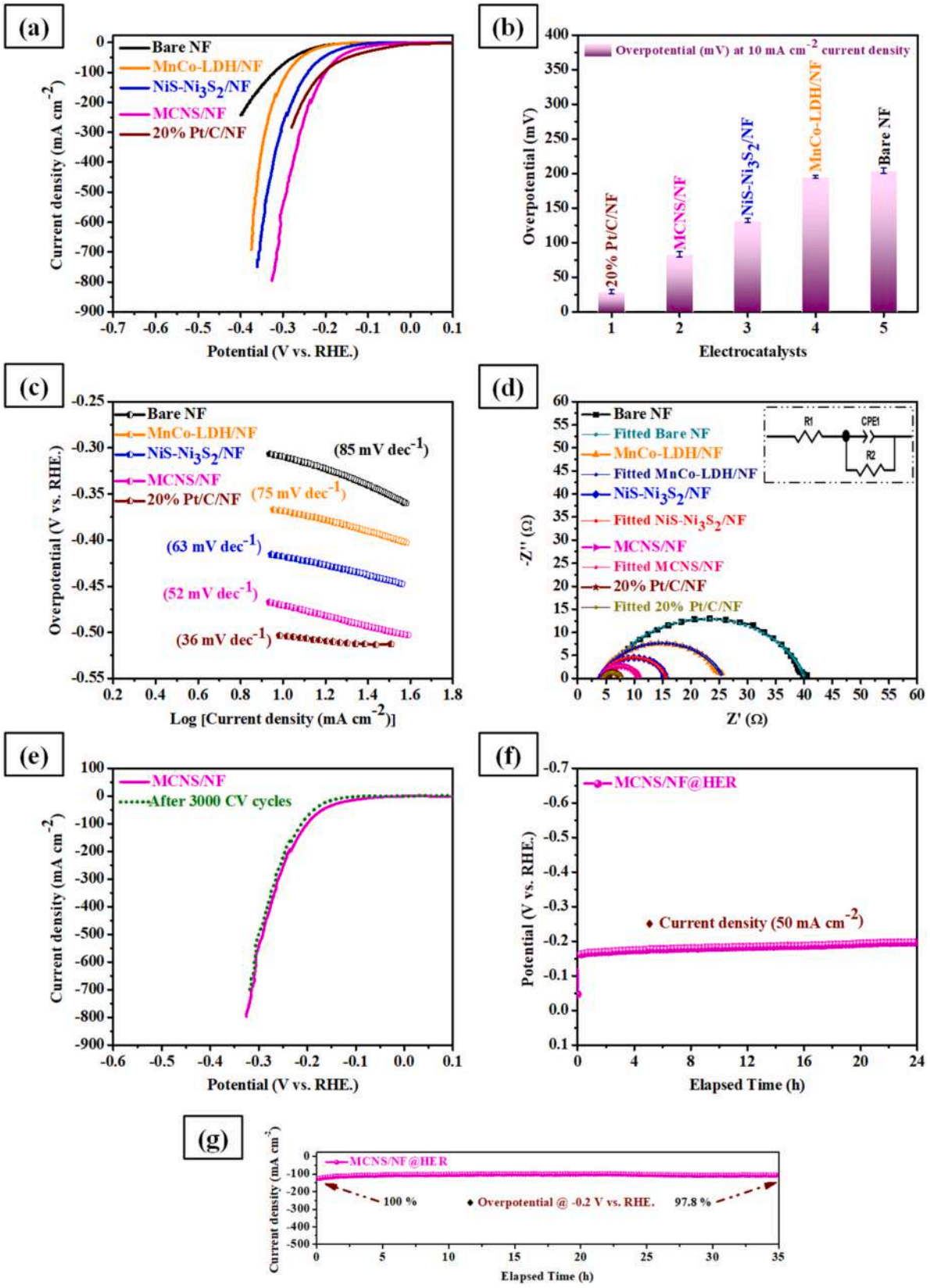

Fig. 7. Electrochemical HER characterization of the different developed electrode materials in 1.0 M KOH electrolyte conditions. LSV polarization profiles (a); comparison of overpotential histogram at 10 mA cm^{-2} (b); estimated Tafel slopes observed by replotting corresponding LSV profiles (c); estimated EIS profiles using Nyquist plots (d); LSV measurements before and after CV cyclic stability test (e); long-term HER chronopotentiometry stability test of the as-fabricated MCNS/NF electrocatalyst conducted for 24 h (f); and long-term HER-chronoamperometric stability assessment of the as-fabricated MCNS/NF electrocatalyst (g).

capacitance (C_{dl}) value by performing the cyclic voltammetry (CV) in the non-faradaic potential region (Fig. S21). As displayed in Fig. S22 and Table S10, MCNS/NF showed a superior C_{dl} value of 3.2 mF cm^{-2} as compared to those of NiS–Ni_3S_2/NF (2.8 mF cm^{-2}), MnCo-LDH/NF (1.64 mF cm^{-2}), bare NF (1.2 mF cm^{-2}), and closer to the benchmark 20% Pt/C/NF (3.68 mF cm^{-2}), respectively. Importantly, to distinguish between geometric and intrinsic catalytic activity, the HER LSV curves were further normalized to ECSA (Fig. S22). After normalization, MCNS/NF still exhibited superior HER performance, which arose not only from the increased number of active sites but also from improved intrinsic activity per active site. To further evaluate the intrinsic catalytic activity, the turnover frequency (TOF) values were calculated at an η of 100 mV based on the estimated number of active sites derived from CV integration (Fig. S23a). The MCNS/NF electrocatalyst exhibited a significantly higher TOF value of $4.32 \times 10^{-4} \pm 1.2 \times 10^{-5}$ s^{-1}, compared to $1.392 \times 10^{-4} \pm 1.5 \times 10^{-5}$ s^{-1} for NiS–Ni_3S_2/NF and $2.82 \times 10^{-5} \pm 3 \times 10^{-6}$ s^{-1} for MnCo-LDH/NF. This pronounced enhancement confirmed that the superior HER performance of MCNS/NF originated from intrinsically higher catalytic efficiency per active site (Fig. S23b). Mass activity analysis further supported the intrinsic catalytic efficiency of the prepared active materials **(Section S5)**. At η of 100 mV, MCNS exhibited a high mass activity of 1.86 ± 0.0025 A g^{-1}, which is significantly higher than NiS–Ni_3S_2 (0.91 ± 0.04 A g^{-1}) and MnCo-LDH (0.13 ± 0.3 A g^{-1}), confirming superior utilization of electroactive sites and enhanced intrinsic HER performance (Fig. S24a). These outcomes indicated that the distinct advantage of the electrocatalysts for HER electrochemical activity stemmed from the exceptional electroactive sites and surface roughness of the marigold flower-like heterogeneous MCNS/NF during the cathodic reaction. Moreover, to investigate cyclic reliability, the comparative analysis of LSV curves for MCNS/NF showed no noticeable variation in current response or η after 3000 CV cycles, further demonstrating the outstanding consistency and resilience of the electrocatalyst during long-term alkaline HER operation (Fig. 7e). Likewise, the long-term operational stability of the electrocatalyst played a critical role in evaluating the practicability under high current density. A 24 h chronoamperometric study was performed at 50 mA cm^{-2} to assess catalyst stability under higher current density conditions (Fig. 7f). Additionally, multi-current chronopotentiometry measurements were further conducted at varying current densities of 10, 20, 30, 40, and 50 mA cm^{-2} for HER over prolonged operation (25 h) to comprehensively evaluate the durability of the electrode under practical working conditions (Fig. S25a). The catalyst exhibited negligible potential fluctuation and maintained stable electrochemical performance across all applied current densities, confirming its excellent long-term operational stability. Furthermore, Fig. 7g exhibited the chronoamperometric response of the MCNS/NF electrocatalyst recorded at a fixed overpotential of −0.2 V vs. RHE for continuous operation in 1.0 M KOH. The catalyst exhibited a highly stable current density with a negligible degradation rate of 0.063% h^{-1} during the initial 35 h of operation. To further evaluate long-term durability under prolonged electrochemical conditions, an extended chronoamperometric stability test was conducted for 110 h at a fixed applied potential of −0.25 V vs. RHE, with a retention percentage of 96.8%, as presented in Fig. S26a. These features prevented structural degradation and maintained reaction kinetics under prolonged, high-current operation, quantitatively confirming the robustness and practical applicability of the MCNS/NF electrocatalyst for alkaline HER. This analysis indicated that the MCNS/NF heterostructure electrode achieved remarkable HER performance, surpassing those of other most recently reported electrocatalysts (Table S11).

3.3.2. Alkaline OER performances

To employ the as-prepared electrocatalysts as bifunctional electrodes for water electrolysis, the multi-step OER performance was further assessed in the same configuration. Firstly, Fig. S19 illustrates the possible reaction pathways during the alkaline OER process. Fig. 8a displays 100% iR-corrected LSV polarization curves of all as-synthesized electrode materials along with the commercial RuO_2. At a current density of 10 mA cm^{-2}, the MCNS/NF heterogeneous nanoarrays exhibited an excellent OER performance with a lower η of 230 mV, which was better than the other controlled electrocatalysts, such as RuO_2/NF, MnCo-LDH/NF, NiS–Ni_3S_2/NF, and bare NF at 270, 285, 297, and 345 mV, respectively. For comparison, Fig. 8b shows the OER η histogram for the controlled electrode materials at a 10 mA cm^{-2} current density (Table S12). As expected, the MCNS/NF heterostructure exhibited better performance due to the strong electronic interaction in the multi-component lattice, thereby considerably enhancing OER kinetics. Fig. 8c illustrates that the subsequent Tafel slopes were used to monitor in-depth OER dynamics of the designed electrocatalysts. A Tafel slope of 95 mV dec^{-1} was obtained for the MCNS/NF, which was remarkably smaller than those of RuO_2/NF (116 mV dec^{-1}), MnCo-LDH/NF (137 mV dec^{-1}), NiS–Ni_3S_2/NF (152 mV dec^{-1}), and bare NF (163 mV dec^{-1}), demonstrated the rapid kinetic rate of MCNS/NF suggesting that the reaction proceeds through a favourable adsorbate evolution mechanism (AEM), where the formation and transformation of oxygenated intermediates represent the rate-limiting processes (Table S12). Moreover, the α values calculated from the corresponding Tafel slopes further confirmed the enhanced OER kinetics of the MCNS/NF electrocatalyst. The α values decreased in the sequence of MCNS/NF (0.62) > RuO_2/NF (0.51) > MnCo-LDH/NF (0.43) > NiS–Ni_3S_2/NF (0.39) > bare NF (0.36), indicating progressively improved electron-transfer behavior (Table S12). The relatively higher α value of MCNS/NF (0.62) reflected more efficient electron transfer during the formation and transformation of oxygenated intermediates, thereby supporting the favourable AEM process. To further investigate the ion/electron transport kinetics at the electrode/electrolyte interface and the electrical properties during the OER, EIS was performed. The MCNS/NF heterostructure demonstrated the lowest R_{ct} value of 10.6 Ω, as depicted in the fitted Nyquist plot using the equivalent circuit model (Fig. 8d, & Table S13), indicating minimal resistance to the interfacial charge transfer redox, and enhanced electrolytic conductivity compared to RuO_2/NF (16.0 Ω), MnCo-LDH/NF (27.8 Ω), NiS–Ni_3S_2/NF (40.0 Ω), and bare NF (70.0 Ω), respectively. The OER superiority of the MCNS/NF heterostructure over the other as-prepared electrocatalysts was further examined through the ECSA by performing the CV technique at the non-redox area (Fig. S25). As shown in Fig. S26 and Table S14, the MCNS/NF exhibited the catalytically relevant ECSA with a C_{dl} of 7.24 mF cm^{-2}, which was superior to the other comparatives of RuO_2/NF (6.2 mF cm^{-2}), MnCo-LDH/NF (5.72 mF cm^{-2}), NiS–Ni_3S_2/NF (5.44 mF cm^{-2}), and bare NF (3.92 mF cm^{-2}). To further distinguish between geometric and intrinsic electrocatalytic activity, the OER LSV curves were normalized to ECSA (Fig. S29). The ECSA-normalized OER LSV curves revealed that MCNS/NF maintained superior intrinsic activity relative to the control electrocatalysts, confirming that its enhanced OER performance originated from intrinsically more active catalytic sites. Furthermore, to assess the intrinsic OER catalytic activity, the TOF values were calculated at an η of 250 mV based on the active site density estimated from CV integration (Fig. S23a). The MCNS/NF electrocatalyst delivered a TOF of $3.408 \times 10^{-4} \pm 0.9 \times 10^{-5}$ s^{-1}, surpassing those of MnCo-LDH/NF ($1.908 \times 10^{-4} \pm 1.2 \times 10^{-5}$ s^{-1}) and NiS–Ni_3S_2/NF ($1.218 \times 10^{-4} \pm 0.6 \times 10^{-5}$ s^{-1}), respectively. This behavior was consistent with the observed OER performance, suggesting that the enhanced activity of MCNS/NF mainly stems from improved intrinsic catalytic efficiency at its active sites (Fig. S23c). Importantly, the intrinsic catalytic efficiency was further validated through mass activity analysis. At η of 250 mV, MCNS/NF delivered a high mass activity of 3.02 ± 0.04 A g^{-1}, which is significantly higher than MnCo-LDH (1.9 ± 0.06 A g^{-1}) and NiS–Ni_3S_2 (1.46 ± 0.02 A g^{-1}), confirming efficient utilization of active sites and superior intrinsic OER performance (Fig. S24b). This analysis demonstrated that broadening the electroactive sites in the MCNS/NF heterostructure improved alkaline OER performance. Moreover, the chronoamperometric test and CV

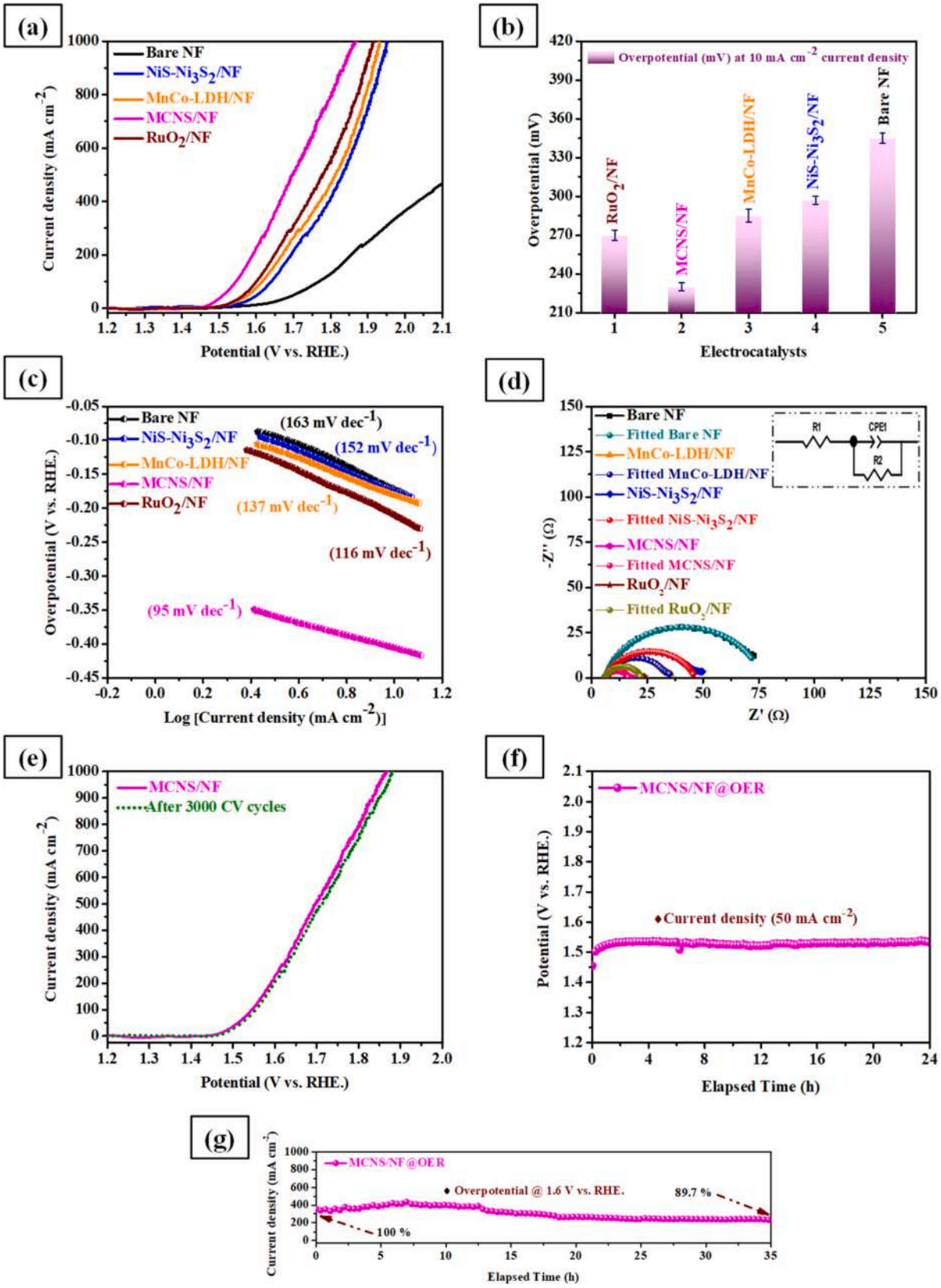

Fig. 8. Electrochemical OER characterization of the different developed electrode materials in 1.0 M KOH electrolyte conditions. LSV polarization profiles (a); comparison of overpotential histogram at 10 mA cm^{-2} (b); estimated Tafel slopes observed by replotting corresponding LSV profiles (c); estimated EIS profiles using Nyquist plots (d); LSV measurements before and after CV cyclic stability test (e); long-term OER chronopotentiometry stability test of the as-fabricated MCNS/NF electrocatalyst conducted for 24 h (f) and long-term OER-chronoamperometric stability assessment of the as-fabricated MCNS/NF electrocatalyst (g).

cycling test were performed to investigate the long-term stability of the MCNS/NF heterostructure. As shown in Fig. 8e, after 3000 CV cycles, the post-polarization LSV curve exhibited no significant change in OER overpotential at 10 mA cm^{-2}, confirming the material's excellent durability in an alkaline medium. The catalyst performance under higher current density conditions was evaluated through a 24 h chronoamperometric study at 50 mA cm^{-2} (Fig. 8f). Moreover, the MCNS/NF heterostructure electrocatalyst exhibited no discernible fluctuation with a degradation rate of 0.29% h^{-1} in current density during continuous operation for 35 h at a fixed applied potential of 1.6 V vs. RHE (Fig. 8g). In order to verify the long-term operational stability, a prolonged chronoamperometric OER test was conducted for 110 h at a constant applied potential of 1.7 V vs. RHE, achieving a retention rate of 85.3%, as shown in Fig. S26b. Multi-current chronopotentiometry measurements for OER were performed at current densities of 10, 20, 30, 40, and 50 mA cm^{-2} over prolonged operation (25 h) to assess the long-term durability of the electrocatalyst (Fig. S25b). The catalyst demonstrated a stable potential response with negligible fluctuation across all applied current densities, confirming its excellent operational robustness under anodic conditions. This outstanding stability can be attributed to the robust hierarchical architecture. These characteristics effectively prevented surface reconstruction or structural degradation, confirming the practical applicability of the MCNS/NF electrocatalyst for prolonged, high-current-density OER in alkaline conditions. These findings manifested that the MCNS/NF can provide a facile delivery of the produced O_2 due to its unique heterogeneous architecture, which served as a novel active center; thus, it outperformed most other previously reported bifunctional electrocatalysts for OER (Table S15).

3.3.3. Alkaline bifunctional-OWS performances

Encouraged by the excellent capabilities of the hierarchical MCNS/NF heterostructure electrocatalyst towards alkaline HER and OER. A symmetric self-standing two-electrode electrolyzer system based on MCNS/NF||MCNS/NF was constructed to examine the near-real OWS activity in 1.0 M KOH (Fig. 9a). Impressively, the constructed water electrolyzer system required a cell voltage of 1.54 V to achieve a current response of 10 mA cm^{-2} (Fig. 9b). Additionally, Table S16 presents a comparative analysis of the cell potential at 10 mA cm^{-2} for the MCNS/NF||MCNS/NF electrode configuration, along with other recently reported non-precious transition-metal-based heterogeneous bifunctional alkaline electrolyzers. To further verify the electrochemical robustness of the MCNS/NF||MCNS/NF symmetric cell electrolyzer for practical utilization, chronoamperometric stability measurements were conducted at different applied voltages of 1.65, 1.7, 1.75, and 1.85 V corresponding to high current densities of 100, 150, 300, 500 mA cm^{-2} for 35 h. As illustrated in Fig.9c and S28a, there was no substantial loss in current density after prolonged operation, demonstrating its exceptional durability, mechanical integrity, and strong electrode-electrolyte interfacial stability in alkaline medium. Additionally, the resulting post-stability LSV curves exhibited negligible voltage shifts and nearly overlapping polarization profiles across the entire current density range, including the high-current-density region (≥100 mA cm^{-2}) (Fig. S28b–S28d). To further evaluate long-term operational durability, the MCNS/NF||MCNS/NF electrolyzer was additionally subjected to an extended chronoamperometric stability test for 110 h at 10 mA cm^{-2} (1.54 V), as presented in Fig. S32. The negligible variation in current density throughout the entire operation, with a degradation rate of 0.04% h^{-1}, confirmed its outstanding long-term stability and structural robustness under practical alkaline OWS conditions. The MCNS/NF||

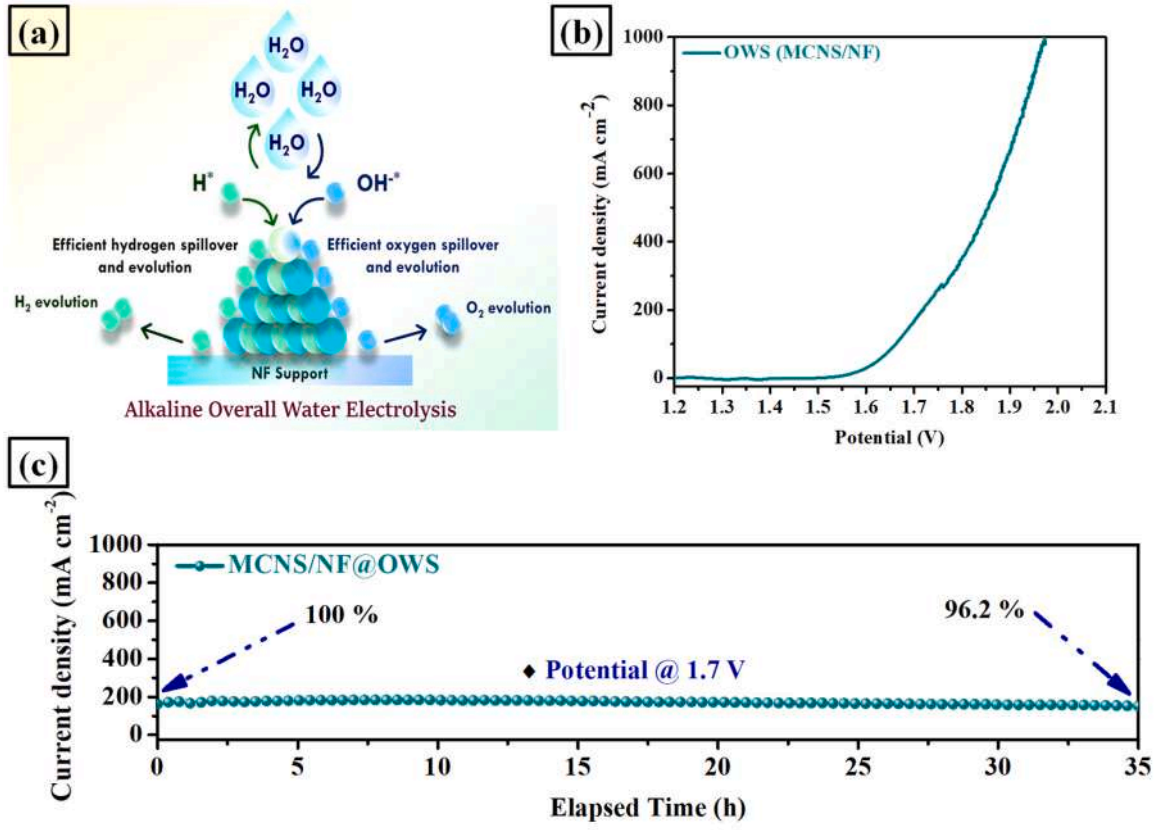

Fig. 9. Electrochemical OWS activity of the constructed symmetric self-standing two electrode alkaline MCNS/NF||MCNS/NF electrolyzer system in 1.0 M KOH electrolyte conditions. Graphical presentation of the hydrogen & oxygen spillover process from cathodic & anodic end (a); estimated bifunctional LSV profile of self-standing two-electrode device (b); and long-term OWS-chronoamperometric stability assessment of the fabricated MCNS/NF||MCNS/NF electrolyzer system (c).

MCNS/NF electrolyzer maintained stable catalytic activity and favourable reaction kinetics under sustained high-load operation, thereby confirming the exceptional robustness, mechanical integrity, strong electrode-electrolyte interfacial stability, and reliability of the hierarchical electrode architecture in alkaline medium. Additionally, to evaluate the faradaic efficiency (FE) of the MCNS/NF||MCNS/NF electrolyzer system, a lab-made H-cell setup was used to capture the evolved H_2 and O_2 gases (Fig. S29). The chronoamperometric approach was implemented on the cell device at a constant voltage of 1.9 V for 1 h. During the experiment, rapid gas bubble production was clearly observed and accumulated in the cylinders, exhibiting a linear upward trend over time, which was nearly consistent with the theoretical stoichiometry of water splitting (Figs. S30–S32). As a consequence, the calculated faradaic efficiencies of the system were found to be 93.02% for H_2, and 91.90% for O_2, along with the H_2 and O_2 volume ratio close to 2:1, confirming predominant utilization of electrical energy to produce H_2 and O_2 via the MCNS/NF heterostructure electrocatalyst for alkaline OWS process.

In light of the obtained outcomes, the heterogeneous nanostructure electrode emerged as a promising electrocatalyst for excellent OWS performance that could be ascribed to the following factors: (i) The design of an exceptional multi-component heterogeneous nanostructure, and the combined effect between the MnCo LDH and NiS–Ni_3S_2 phases, which reinforced the electrochemical water redox activity by optimizing the electronic properties of the catalytically active centers. (ii) The contribution of multiple transition metals (Mn, Co, and Ni) and non-metal (S) could tailor the electronic structural integrity, which leads to efficient charge transfer capacity and enhanced the resistance to degradation, allowing for both accelerating the OWS reaction kinetics and the ability to withstand long-term structural integrity. (iii) The concentrated coupling in this heterogeneous system facilitated the equilibrium adsorption of a negatively charged oxygen atom in the positively charged MnCo-LDH nanosheets; alternatively, negatively charged NiS–Ni_3S_2 nanoarrays have an excellent potential for creating hydrogen bonds with adsorbed hydrogen intermediates, which efficiently enhanced mass diffusion and generated synergism to assist the cleavage of H–OH bonds. Thus, this electronic reconstruction enhanced electrical conductivity and charge transfer kinetics, thereby lowering the required overpotentials and Tafel slopes, while simultaneously reducing the charge-transfer resistance observed in EIS. As a consequence, these characteristics indicate that the hierarchical MCNS/NF heterogeneous system has substantial potential for alkaline OWS applications, suggesting a feasible approach for green H_2 generation (Tables S17–S18).

3.4. Analysis of post-studied electrode materials

Considering the excellent alkaline HER, OER, and OWS electrochemical performance along with the outstanding durability of the MCNS/NF hybrid heterostructure, further post-physicochemical characterizations were performed to examine the structural, morphological, and chemical states of the well-designed electrode material. As shown in the FE-SEM, EDX, HR-TEM, SAED, and HAADF-STEM results shown in Figs. S37–S44, it was found that there is no significant change in the geometrical morphology, as well as in lattice fringes along with the interplanar distances, thereby confirming pronounced structural stability of the electrocatalyst with the preserved elements of Mn, Co, Ni, S, and O throughout the nanoflower structure. Furthermore, the post-XRD pattern and post-FT-IR results showed no discernible variation in the 2θ degree and chemical bonding of the functional groups, along with no emergence of new crystalline phases, suggesting consistency in its phase purity and its limited susceptibility to the reaction conditions that prevailed over an extended period of operation (Figs. S45–S47). In addition, the supremacy of the heterogeneous electrocatalyst, as well as the chemical states of the metal components, was further recognized by XPS analysis. The XPS survey spectra for both post-HER and post-OER materials revealed no obvious variation in peak positions of the respective elements compared to the virgin one (Fig. S48 & Tables S19–22). The high-resolution XPS spectra of Mn 2p, Co 2p, Ni 2p, S 2p, and O 1s displayed no noticeable change in binding energy, compared to the pre-HER state, governing the inherent conservancy in the chemical configuration as well as the surface chemistry throughout the HER testing process (Fig. S49, Table S19, & Table S21). Nevertheless, as shown in Fig. S50 and Table S22, the XPS spectra of Mn 2p, Co 2p, and S 2p demonstrated a noticeable diminution of peak intensities, which depicts the partial dissolution of the metal ions under the highly oxidative OER process in alkaline conditions, and is also attributed to the generation of oxyhydroxide (-OOH) reactive species in conjunction with the heterointerface. In addition, Mn 2p, Co2p, Ni 2p, S 2p, and O 1s XPS spectra showed a slight shift towards a lower binding energy after long-term OER operation; this phenomenon corresponded to the mild surface reconstruction, but inferred an increase of $O_{M\text{-}O}$ (lattice oxygen) species, which, improve the synergistic effect, thereby facilitating the commendable anodic activity, along with outstanding electrochemical stability (Fig. S50, Table S20, & Table S22). Thus, these overall findings highlight the exceptional electrochemical robustness and excellent intrinsic electrocatalytic activity of the MCNS/NF heterostructure for alkaline water splitting to produce green H_2.

4. Conclusions

In the overview, a typical electrocatalyst engineering strategy was executed to develop a defect-rich 3D hierarchical MCNS/NF electrocatalyst with an artistic heterogeneous nanostructure using a controlled two-step hydrothermal process. Morphological and structural characterizations using techniques such as FE-SEM, EDX, PXRD, FT-IR, HR-TEM, and SAED, combined with advanced AC-HAADF-STEM imaging, EELS analysis, and line-scan elemental mapping, confirmed the successful formation of a multi-component heterostructure. The NiS–Ni_3S_2 nanoarrays integrated with MnCo-LDH nanosheets provided abundant and accessible electroactive sites. This architecture delivered exceptional performance in diverse electrochemical applications, functioning as an efficient bifunctional electrocatalyst for both HER and OER in sustainable energy conversion. As a result, the MCNS/NF heterostructure achieved an η of 83 and 230 mV for HER and OER at a current density of 10 mA cm^{-2}, in addition to smaller Tafel slopes of 52 and 95 mV dec^{-1}, along with excellent durability in 1.0 M KOH, respectively. Notably, when the multi-component heterostructure was effectively employed as a two-electrode system assembly for OWS, the electrolyzer cell delivered a cell voltage as small as 1.54 V at the respective current density of 10 mA cm^{-2} with remarkable faradaic efficiencies of 93.02% for H_2 & 91.90% for O_2, and exceptional durability that was superior to that of the earlier reported dual-functional noble metal-free transition metal-based electrocatalysts in 1.0 M KOH. By persisting in research, this work may pave the way for new insights into the development of highly efficient electrocatalysts and their engineering strategies, which would be promising for next-generation bifunctional applications in energy conversion systems to meet future energy demands.

CRediT authorship contribution statement

Ujjwal Phadikar: Conceptualization, Data curation, Formal analysis, Investigation, Methodology, Validation, Writing – original draft. **Anjan Chakraborty:** Data curation, Formal analysis, Investigation, Methodology, Validation. **Srijib Das:** Data curation, Formal analysis, Investigation, Software. **Debasish Mondal:** Data curation, Formal analysis, Investigation. **Sukanya Bhattacharjee:** Data curation, Formal analysis, Investigation. **Debasis Dhak:** Data curation, Formal analysis, Investigation, Resources. **Naresh Chandra Murmu:** Formal analysis, Funding acquisition, Investigation, Project administration, Resources. **Tapas Kuila:** Conceptualization, Data curation, Formal analysis, Funding acquisition, Investigation, Project administration, Resources,

Supervision, Writing – review & editing.

Declaration of competing interest

The authors declare the following financial interests/personal relationships which may be considered as potential competing interests: Tapas Kuila reports financial support was provided by Central Mine Planning and Design Institute Limited. Tapas Kuila reports financial support was provided by Council of Scientific & Industrial Research. Ujjwal Phadikar reports was provided by Council of Scientific & Industrial Research. If there are other authors, they declare that they have no known competing financial interests or personal relationships that could have appeared to influence the work reported in this paper.

Acknowledgments

This work received financial assistance from the CMPDI Project (Sanction No. CU-61/04 dated January 8, 2024). T.K. is thankful to the Council of Scientific & Industrial Research, New Delhi, through the Project HCP-54 (Sanction No. 4/1/WTW/2023-IMD dated 28/08/2023). U.P. is grateful to the CSIR, Govt. of India, for the CSIR SRF-Direct Fellowship File No: 31/0019(23253)/2025-EMR-I. The authors are thankful to SATHI Foundation, IIT Kharagpur, for providing AC-HAADF-STEM and EELS facilities.

Appendix A. Supplementary data

Supplementary data to this article can be found online at https://doi.org/10.1016/j.ijhydene.2026.155916.

References

[1] Nguyen TTA, Duong NTA, Sidra S, Kim DH, Kim NH, Tran DT, Lee JH. Electronic and active sites reconstruction endowed by atomic ruthenium-modulated V_2P-MoP heterointerfaces-hybridized N-doped carbon for enhanced water splitting. J Mater Sci Technol 2026;263:189–99. https://doi.org/10.1016/j.jmst.2025.11.007.

[2] Balamurugan J, Austeria PM, Kim JB, Jeong E-S, Huang H-H, Kim DH, Koratkar N, Kim SO. Electrocatalysts for zinc-air batteries featuring single molybdenum atoms in a nitrogen-doped carbon framework. Adv Mater 2023;35:2302625. https://doi.org/10.1002/adma.202302625.

[3] Du F, Shi L, Zhang Y, Li T, Wang J, Wen G, Alsaedi A, Hayat T, Zhou Y, Zou Z. Foam-like Co_9S_8/Ni_3S_2 heterostructure nanowire arrays for efficient bifunctional overall water-splitting. Appl Catal B Environ 2019;253:246–52. https://doi.org/10.1016/j.apcatb.2019.04.067.

[4] Li X, Dong K, Sidra S, Kim DH, Tran DT, Kim NH, Lee JH. Atomic Pt-Promoted hierarchical CoP@CNTs-Bridged CeO_2-CoP heterostructure-based hollow microcubes for water electrolysis. Small 2025;21:e07407. https://doi.org/10.1002/smll.202507407.

[5] Chauhan P, Patel AB, Solanki GK, Sumesh CK, Soni SS, Late DJ, Patel V, Pathak VM. Engineered interfaces of WSe_2/rhenium doped $SnSe_2$ heterostructures nanosheet arrays for superior hydrogen generation and flexible supercapacitor. Mater Today Chem 2022;26:101079. https://doi.org/10.1016/j.mtchem.2022.101079.

[6] Thakur A, Devi P. Paper-based flexible devices for energy harvesting, conversion and storage applications: a review. Nano Energy 2022;94:106927. https://doi.org/10.1016/j.nanoen.2022.106927.

[7] Liu X, Li Y, Cao Z, Yin Z, Ma T, Chen S. Current progress of metal sulfides derived from metal-organic frameworks for advanced electrocatalysis: potential electrocatalysts with diverse applications. J Mater Chem A 2022;10:1617–41. https://doi.org/10.1039/D1TA09925F.

[8] Shembade UV, Gurav SR, Gurav AN, Wategaonkar SB, Padalkar NS, Sonkawade RG, Park JP, Moholkar AV. Exploring the effect of concentration on hydrothermally synthesized mesoporous spherical nanoflowers of bismuth tungstate for hybrid supercapacitor and water-splitting applications. J Energy Storage 2024;89:111679. https://doi.org/10.1016/j.est.2024.111679.

[9] Liu J-C, Huang Z-H, Ma T-Y. Aqueous supercapacitor with ultrahigh voltage window beyond 2.0 volt. Small Struct 2020;1:2000020. https://doi.org/10.1002/sstr.202000020.

[10] Phadikar U, Sahoo R, Das MC, Kuila T. A chemically robust SIFSIX MOF as electrocatalyst in alkaline hydrogen evolution reaction (HER). Int J Hydrogen Energy 2025;117:135–45. https://doi.org/10.1016/j.ijhydene.2025.03.120.

[11] Phadikar U, Das S, Bolar S, Kundu A, Kolya H, Kang C-W, Murmu NC, Kuila T. Sulfur scrambling assisted in-situ growth of 3D - hierarchical $FeNi_2S_4$@Mo-doped Ni_3S_2/NF nanosheet arrays: a stellar performer towards alkaline water electrolysis. J Power Sources 2023;576:233244. https://doi.org/10.1016/j.jpowsour.2023.233244.

[12] Song Z, Miao L, Ruhlmann L, Lv Y, Zhu D, Li L, Gan L, Liu M. Self-assembled carbon superstructures achieving ultra-stable and fast proton-coupled charge storage kinetics. Adv Mater 2021;33:2104148. https://doi.org/10.1002/adma.202104148.

[13] Pan Z, Tang Z, Sun D, Zhan Y. Hierarchical $NiCo_2S_4$@$NiMoO_4$ nanotube arrays on nickel foam as an advanced bifunctional electrocatalyst for efficient overall water splitting. Electrochim Acta 2022;436:141393. https://doi.org/10.1016/j.electacta.2022.141393.

[14] Zheng E, Zheng Q, Liu M, Fu S, Liang L. Chlorine corrosion of ubiquitous rust towards low-cost, efficient and free-standing electrocatalysts for overall water splitting. New J Chem 2024;48:18908–16. https://doi.org/10.1039/D4NJ03610G.

[15] Zhang Q, Zhong H, Meng F, Bao D, Zhang X, Wei X. Three-dimensional interconnected $Ni(Fe)O_xH_y$ nanosheets on stainless steel mesh as a robust integrated oxygen evolution electrode. Nano Res 2018;11:1294–300. https://doi.org/10.1007/s12274-017-1743-8.

[16] Surendran S, Selvan RK. Growth and characterization of 3D flower-like β-NiS on carbon cloth: a dexterous and flexible multifunctional electrode for supercapattery and water-splitting applications. Adv Mater Interfac 2018;5:1701056. https://doi.org/10.1002/admi.201701056.

[17] Afshan M, Kumar N, Das S, E m H, Rani D, Sharangi S, Pahuja M, Siddiqui SA, Rani S, Chaudhary N, Bera C, Ghosh K. Electronic modulation of MOF-engineered bimetallic phosphides for cost-effective ampere-level water splitting and continuous hydrogen production via supercapacitor integration. J Energy Chem 2025;108:221–38. https://doi.org/10.1016/j.jechem.2025.04.018.

[18] Y. Zheng, J. Fan, J. Zou, T. Wen, H. Wang, Black phosphorene: a rising 2D platform for hydrogen evolution electrocatalysis, Adv Funct Mater. n/a (n.d.) e75413. https://doi.org/10.1002/adfm.75413.

[19] T. Wen, Y. Zheng, J. Zou, H. Wang, Advancements and challenges in metal selenides for electrocatalytic H_2 evolution, J Mater Chem A 14 (2026) 9138–9176. https://doi.org/10.1039/D5TA08735J.

[20] Phadikar U, Panda B, Das S, Dhak D, Kundu A, Murmu NC, Kuila T. Tailoring the numerous intimate sites between the interfaces of CoCu-LDH@$FeNi_2S_4$-$FeNiS_2$@$CoNi_2S_4$/NF heterogeneous electrode: monitoring the synergistic interplay and connecting the dots for alkaline water electrolysis. Int J Hydrogen Energy 2025;129:75–90. https://doi.org/10.1016/j.ijhydene.2025.04.325.

[21] Phadikar U, Sanyal G, Das S, Kundu A, Kuila C, Murmu NC, Chakraborty B, Kuila T. Unique multi-hetero-interface engineering of Fe-Doped Co-LDH@MoS_2-Ni_3S_2 nanoflower-based electrocatalyst for overall water-splitting: an experimental and theoretical investigation. ChemSusChem 2024;17:e202400821. https://doi.org/10.1002/cssc.202400821.

[22] Wen T, Yang M, Zou J, Wang H. Localized phosphorization synthesis of vacancy-rich $NiCo_2O_4$/NiCoP urchin-like heterojunction for alkaline electrocatalytic water splitting. Ind Eng Chem Res 2025;64:9209–16. https://doi.org/10.1021/acs.iecr.5c00751.

[23] Li X, Wen T, Zheng Y, Zou J, Wang H. Interfacial Ti-S bond confers NiS_2/Ti_3CNCl_2 MXene heterojunction efficient oxygen evolution electrocatalytic performance. J Power Sources 2025;653:237772. https://doi.org/10.1016/j.jpowsour.2025.237772.

[24] Le QTT, Nguyen TT, Tran KD, Ngo QP, Tran DT, Kim NH, Lee JH. Regulating the d-band center of high valent Ru-doped NiCoP for efficient electrocatalyst in robust anion exchange membrane water electrolysis devices. Chem Eng 2025;521:166378. https://doi.org/10.1016/j.cej.2025.166378.

[25] Devi TA, Bollu M, Sidra S, Kim DH, Tran DT, Kim NH, Lee JH. Advanced interface engineering of manganese–doped biphasic nickel-cobalt phosphide heterostructures enables high-efficiency overall water splitting in freshwater and seawater media. J Colloid Interface Sci 2026;704:139348. https://doi.org/10.1016/j.jcis.2025.139348.

[26] Zheng Y, Song C, Zou J, Fan J, Wen T, Wang H. In-situ growth of Ni_2P nanocrystals on black phosphorus nanosheets endows an effective built-in electric field for enhanced H_2 production in anion exchange membrane water electrolyzers. Chem Eng J 2025;524:169189. https://doi.org/10.1016/j.cej.2025.169189.

[27] Xu Z, Wu Z-S. Scalable production of high-performance electrocatalysts for electrochemical water splitting at large current densities. eScience 2025;5:100334. https://doi.org/10.1016/j.esci.2024.100334.

[28] Javed N, Khan IA, Farid A, Aftab K. Transition metal sulfide electrocatalysts for water splitting: bridging computational design and experimental advancements. J Power Sources 2025;656:238057. https://doi.org/10.1016/j.jpowsour.2025.238057.

[29] Wen T, Zheng Y, Wang H, Zou J. Constructing black phosphorus nanosheet/$CoNiSe_2$ nanoflower heterojunction with effective built-in electric field for robust H_2 evolution in anion exchange membrane water electrolyzer. Appl Catal, B 2025;378:125588. https://doi.org/10.1016/j.apcatb.2025.125588.

[30] Zhang B, Shan J, Wang W, Tsiakaras P, Li Y. Oxygen vacancy and core–shell heterojunction engineering of anemone-like CoP@CoOOH bifunctional electrocatalyst for efficient overall water splitting. Small 2022;18:2106012. https://doi.org/10.1002/smll.202106012.

[31] Majumdar A, Tran KD, Prabhakaran S, Kim DH, Tran DT, Kim NH, Lee JH. Strain engineering of Ru–Co_2Ni nanoalloy encapsulated with carbon nanotubes for efficient anion and proton exchange membrane water electrolysis. Adv Funct Mater 2025;35:2420517. https://doi.org/10.1002/adfm.202420517.

[32] Huang L, Wei M, Qi R, Dong C-L, Dang D, Yang C-C, Xia C, Chen C, Zaman S, Li F-M, You B, Xia BY. An integrated platinum-nanocarbon electrocatalyst for efficient oxygen reduction. Nat Commun 2022;13:6703. https://doi.org/10.1038/s41467-022-34444-w.

[33] Li S, Luo Y, Wang C, Wu M, Xue Y, Yang J, Li L. A novel hierarchical core-shell structure of $NiCo_2O_4$@NiCo-LDH nanoarrays for higher-performance flexible all-

solid-state supercapacitor electrode materials. J Alloys Compd 2022;920:165986. https://doi.org/10.1016/j.jallcom.2022.165986.
[34] Li X, Qin Y, Zhang B, Zhang B, Zhao R, Li J, Zhao D, Miao L. Rose-like NiFe-LDH/MoS_2 electrocatalysts achieve 1000 mA cm^{-2} OER with enhanced charge transfer and seawater stability. Cryst Growth Des 2025;25:8616–30. https://doi.org/10.1021/acs.cgd.5c01006.
[35] Yun TG, Heo Y, Bin Bae H, Chung S-Y. Elucidating intrinsic contribution of d-orbital states to oxygen evolution electrocatalysis in oxides. Nat Commun 2021;12:824. https://doi.org/10.1038/s41467-021-21055-0.
[36] He Y, Liu X, He K, Kamyab H, Gnanasekaran L, Anjana PM, Aminabhavi TM, Vasseghian Y, Hojjati-Najafabadi A. High-performance supercapacitors based on NiMn layered double hydroxides/Ni_3S_2 nanocomposite. J Power Sources 2025;634:236465. https://doi.org/10.1016/j.jpowsour.2025.236465.
[37] Yin X, Yang L, Gao Q. Core–shell nanostructured electrocatalysts for water splitting. Nanoscale 2020;12:15944–69. https://doi.org/10.1039/D0NR03719B.
[38] He Y, Li L, He X, Liu C, Aminabhavi TM, Vasseghian Y, Hojjati-Najafabadi A. Heterostructured nanocoral-like Co(OH)F@NiCo-LDH/Co_9S_8 nanocomposites as electrodes for supercapacitors. ACS Appl Nano Mater 2024;7:12701–10. https://doi.org/10.1021/acsanm.4c01226.
[39] Paul A, Samanta P, Kolya H, Kang C-W, Murmu NC, Kuila T. Rational design of asymmetric aqueous supercapacitor based on the composites of reduced graphene oxide with manganese-doped nickel sulfide-tin sulfide as positive electrode and manganese sulfide negative electrode. J Power Sources 2023;580:233352. https://doi.org/10.1016/j.jpowsour.2023.233352.
[40] Zou X, Zhang Y. Noble metal-free hydrogen evolution catalysts for water splitting. Chem Soc Rev 2015;44:5148–80. https://doi.org/10.1039/C4CS00448E.
[41] Deng J, Li H, Xiao J, Tu Y, Deng D, Yang H, Tian H, Li J, Ren P, Bao X. Triggering the electrocatalytic hydrogen evolution activity of the inert two-dimensional MoS_2 surface via single-atom metal doping. Energy Environ Sci 2015;8:1594–601. https://doi.org/10.1039/C5EE00751H.
[42] Dang L, Liang H, Zhuo J, Lamb BK, Sheng H, Yang Y, Jin S. Direct synthesis and anion exchange of Noncarbonate-Intercalated NiFe-Layered double hydroxides and the influence on electrocatalysis. Chem Mater 2018;30:4321–30. https://doi.org/10.1021/acs.chemmater.8b01334.
[43] Lv W, Mei Q, Fu H, Xiao J, Du M, Zheng Q. A general strategy for the synthesis of layered double hydroxide nanoscrolls on arbitrary substrates: its formation and multifunction. J Mater Chem A 2017;5:19079–90. https://doi.org/10.1039/C7TA05556K.
[44] Hou J, Sheng Y, Bi D, Chen N, Lai Q, Liang Y. Interface engineering of crystalline-amorphous heterostructures with strong electronic interactions for efficient alkaline overall water splitting. J Alloys Compd 2024;977:173447. https://doi.org/10.1016/j.jallcom.2024.173447.
[45] Tang C, Zhang R, Lu W, He L, Jiang X, Asiri AM, Sun X. Fe-Doped CoP nanoarray: a monolithic multifunctional catalyst for highly efficient hydrogen generation. Adv Mater 2017;29:1602441. https://doi.org/10.1002/adma.201602441.
[46] Lu J, Ren L, Li C, Liu H. A reasonable design of $MnCo_2S_4$ and activated carbon composite as cathode catalyst to improve the power output of microbial fuel cells. Catal Lett 2024;154:2340–52. https://doi.org/10.1007/s10562-023-04481-1.
[47] Gong J, Wang X, W H, Dong X, Li J, Yang F, Yuan A, Ji H. MnCo-Layered double hydroxides nanosheets supported Pd nanoparticles for complete catalytic oxidation of formaldehyde at room temperature. Appl Surf Sci 2022;606:154702. https://doi.org/10.1016/j.apsusc.2022.154702.
[48] Raja AS, Sasikumar R, Chen S-M, Kim B. Unveiling the synergistic effect of MnCo LDH adorned $MnCo_2S_4$ nanocomposite as efficient bifunctional electrode for asymmetric supercapacitor and overall water splitting. Small 2025;21:e2411728. https://doi.org/10.1002/smll.202411728.
[49] Kumbhar KR, Redekar RS, Tarwal NL. Investigating the effect of the electrolyte variation on the supercapacitor performance of hydrothermally synthesized cobalt-manganese layered double hydroxide nanospikes. J Energy Storage 2026;146:119854. https://doi.org/10.1016/j.est.2025.119854.
[50] Sathya Sai KN, Darsan AS, Wang K, Pandikumar A, Venkatakrishnan SM, Hong Z. OH-enriched NiS/Ni_3S_2-Zr heterostructure for overall water splitting performance in alkaline media. ACS Appl Nano Mater 2024;7:11931–41. https://doi.org/10.1021/acsanm.4c01502.
[51] Kumari S, Gautam A, Mitra R, Biswas K, Halder A. Understanding the performance of Ni_3S_2/NiO heterojunction as a bifunctional electrocatalysts for 3000-hour stable splitting of untreated river water. Chem Eng J 2026;535:175351. https://doi.org/10.1016/j.cej.2026.175351.
[52] He W, Zhang R, Cao D, Li Y, Zhang J, Hao Q, Liu H, Zhao J, Xin HL. Super-hydrophilic microporous $Ni(OH)_x/Ni_3S_2$ heterostructure electrocatalyst for large-current-density hydrogen evolution. Small 2023;19:2205719. https://doi.org/10.1002/smll.202205719.
[53] Wang Z, Hu Y, Liu W, Xu L, Guan M, Zhao Y, Bao J, Li H. Manganese-modulated cobalt-based layered double hydroxide grown on nickel foam with 1D-2D-3D heterostructure for highly efficient oxygen evolution reaction and urea oxidation reaction. Chem Eur J 2020;26:9382–8. https://doi.org/10.1002/chem.202001055.
[54] Li B, Dai L, Su G, Xia Z, Ye Y, Li Z. Construction of defective MnCo-LDH nanoflowers with high activity for overall water splitting. Fuel 2024;364:130961. https://doi.org/10.1016/j.fuel.2024.130961.
[55] Das S, Dey S, Phadikar U, Kolya H, Kang C-W, Murmu NC, Kuila T, Kundu A. Probing the synergistic effect of metal–organic framework derived Co-Nx rich interwoven hierarchical porous carbon tube encapsulated dual redox active nanoalloy for high-performance Zn-air battery and supercapacitor applications. J Colloid Interface Sci 2025;683:818–32. https://doi.org/10.1016/j.jcis.2024.12.105.
[56] Bhattacharjee S, Phadikar U, Panda B, Dhak D, Murmu NC, Kuila T. Bifunctional CrSe@$FeSe_2$ heterostructure with interface synergy and vacancy engineering for enhanced alkaline water splitting. Chem Mater 2026;38:2989–3000. https://doi.org/10.1021/acs.chemmater.6c00145.